Università degli studi di Padova

DIPARTIMENTO DI FISICA E ASTRONOMIA
Corso di Laurea in Astronomia

TESI DI LAUREA

Statistical analysis of the first results of the SPHERE GTO Survey

Candidato:
Raffaele Stefano Cattolico
Matricola 1105708

Relatori:
Ch.mo Prof. SERGIO ORTOLANI
Correlatore: Dott. RAFFAELE GRATTON
Correlatore: Dott. SILVANO DESIDERA
Correlatrice: Dott. MARIANGELA BONAVITA
Controrelatore: Prof. GIAMPAOLO PIOTTO

Anno Accademico 2015-2016

Ad Andrea

Riassunto

Questa tesi descrive l'analisi statistica delle prime 88 stelle osservate dal canale scientifico IFS (Integral-Field-Spectrograph) nell'ambito della survey SHINE su SPHERE, uno spettro-polarimetro ad alto-contrasto ottimizzato per la ricerca di esopianeti. L'obiettivo finale é porre dei vincoli sulla frequenza dei pianeti giganti a grandi separazioni dalla stella ed eventualmente sul loro meccanismo di formazione.

Nel primo capitolo introduciamo le due principali teorie volte a spiegare il meccanismo di formazione dei pianeti giganti: il "Core Accretion" e il "Disk Instability".

Nel secondo capitolo introduciamo un descrizione del metodo utilizzato per scoprire giovani pianeti giganti, ovvero il direct imaging e nel medesimo capitolo presentiamo lo strumento ottimizzato per eseguire tale tecnica: SPHERE.

Nel terzo capitolo si introduce la survey SHINE che sfrutta il tempo garantito del consorzio SPHERE e che é attualmente in corso, la selezione del target e infine i risultati dei primi due semestri di tale survey.

Nel quarto capitolo descriviamo il formalismo utilizzato per l'analisi statistica e, in particolare, il codice Quick-MESS (Quick-Multi-purpose Exoplanet Simulation System) utilizzato. Esso é un codice alternativo ai classici tool Monte-Carlo per l'analisi statistica di immagini di esopianeti.

Nel quinto capitolo presentiamo i risultati della nostra analisi e infine, nel sesto capitolo, confrontiamo i nostri risultati con quelli presenti in letteratura.

Essendo un'indagine ancora esplorativa molti candidati finora trovati da SPHERE richiedono ancora ulteriori conferme. Solo circa un 1/4 dei target sono stati osservati e l'analisi in questo lavoro di tesi fornirá un primo test sulla metodologia che si prevede applicare una volta che la survey sará terminata.

In questo lavoro abbiamo dimostrato che i dati attuali sono compatibili con le distribuzioni di massa e di semiassi maggiori di pianeti giganti, dedotti dalle velocitá radiali, per separazioni minori di $10 - 20$ AU. Il picco della distribuzione dei pianeta giganti deve quindi essere ad una separazione non molto maggiore della snow-line, in accordo con il recente risultato ottenuto da Bryan et al. (2016) che utilizzano una combinazione di dati ottenuti sia dal metodo delle velocitá radiali che dall'immagine diretta.

Il nostro criterio di selezione del target é nettamente diverso rispetto la selezione su cui lavorano Bryan et al., infatti il nostro

target selection pone particolare attenzione sulla scelta di stelle giovani, senza alcuna assunzione sulla presenza o meno di un compagno. Nonostante la differenza del campione osservato, la frequenza di pianeti finora rilevati nella nostra indagine si presenta compatibile con un'estrapolazione dei risultati di Bryan et al. entro 1σ di livello di confidenza.

Il completamento della survey permetterá di ridurre, all'incirca metá, l'attuale barra di errore e quindi migliorare la stima della frequenza dei pianeti giganti a grandi separazioni (> 10 AU). Questo sará sufficiente a dimostrare se il valore di tale frequenza sia alto, come previsto dall'analisi di Bryan et al., o inferiore come dai nostri dati preliminari.

Infine proponiamo una distribuzione della frequenza dei pianeti giganti in funzione della separazione. Il picco della distribuzione, in accordo con i dati delle velocitá radiali e della survey SHINE, dovrebbe presentarsi leggermente fuori dalla snow-line, proprio come previsto da uno scenario di core-accretion. Inoltre si nota che la posizione di Giove e Saturno risulta compatibile col picco della distribuzione proposta, mostrando quindi che il Sistema Solare, nella distribuzione dei pianeti giganti, non rappresenta un'eccezione.

Abstract

This dissertation reports about a statistical analysis of the first 88 targets observed by the science channel IFS (Integral-Field-Spectrograph) during the SPHERE Guaranteed Time Survey (GTO). The final goal of this work is to put some initial constraints on the frequency of giant planets in wide orbits, on their mass distribution, on their semi-major axis distribution and possibly on the formation mechanism.

In the first chapter we briefly present the two theories aimed at explaining the planet formation mechanism: the "core accretion" and the "disk instability".

In the second chapter we introduce the direct-imaging technique to discover young and self-luminous exoplanets and in the same chapter we present a new instrument optimized to perform direct imaging: SPHERE a Spectro-Polarimetric High-contrast-Exoplanet-REsearch.

In the third chapter we describe the Guaranteed Time of Observation (GTO) survey SHINE, which is currently ongoing on SPHERE, the target selection and finally the results of the first two semesters of the survey.

In the fourth outline we describe the statistical formalism used for the analysis and in particular the Quick-MESS code (Quick Multi-purpose Exoplanet Simulation System): a fast alternative code to the classic Monte-Carlo tools for the statistical analysis of exoplanet direct imaging surveys.

The results of our analysis are given in the fifth chapter and finally we compare our data with results from other surveys in sixth chapter.

Although still exploratory, because the candidates so far found with SPHERE still require confirmation and only about 1/4 of the targets have been observed, this analysis will provide a first test of the methodology we plan to use once the survey is completed and some very early results. We show that current data are compatible with distributions, from the radial velocities, with only few planets beyound $10 - 20$ AU. The peak of the giant planet distribution should then be at a separation not much larger than the snow-line, in agreement with the very recent result obtained by Bryan et al. (2016) from a combination of a radial velocity and the direct imaging data. This is interesting because the selection criteria used in our survey is very different, focusing on young objects and is not biased versus system with closer planets. On the other hand, the number of planets so far detected in our survey, while still compatible with

an extrapolation of the results by Bryan et al., is at the lower limit of the acceptable range. Completion of the SPHERE survey will roughly reduce at half the current error bar in the frequency of planets at large separations (> 10 AU). This will be enough to show if this frequency is as high as expected from Bryan et al. analysis, or lower as suggested by our preliminary data.

Finally, we propose a distribution of the frequency of giant planets versus the separations. The peak of distribution, in agreement with RV and SHINE data, should be slightly out of the snow-line as predicted by the core accretion scenario. Furthermore we note that the positions of Jupiter and Saturn are compatible with the peak of the overall distribution of giant planets, showing that on this respect the Solar System does not represent an exception.

Contents

1 Introduction

Twenty-one years ago astronomers announced the discovery of 51 Pegasi *b*, the first confirmed planet orbiting a Sun-like star. This hellish gas giant orbits just beyond the searing heat of its parent star, and it opened astronomer's eyes to the astonishing range of alien worlds that exist throughout the Galaxy. The tally of known extrasolar planets now stands at 2087[1] with nearly 4700 more candidates waiting to be confirmed.

The study and characterization of exoplanets is one of the most controversial topic in the astronomical research. Studying extrasolar planets means, inevitably, to understand solar systems like our own, and so to investigate its origin and history, which is far from being completely understood.

One of the primary goals of Extrasolar Planet Science is a better understanding of the mechanism of formation and evolution of planetary system. In order to discern this mechanism we focus on the giant planets: the study of the evolution of the gaseous giants is useful to understand the formation of a planetary system. One of the fundamental observational parameters is the frequency of planets as a function of mass and separation. Obviously, in a global evolutionary analysis, many others perturbative phenomena like planetary migrations, resonances and so on need to be considered. Understanding the formation of giant planets with substantial gaseous envelopes forces us to confront the physics of the gas within the protoplanetary disk.

1.1 Planets formation mechanism

In this chapter we introduce the two competing models: the "core accretion" scenario (Pollack et al. 1996) and the "disk instability" scenario (Cameron, 1978). In the Core Accretion model the acquisition of a massive envelope of gas is the final act of a process that begins with the formation of a core of rock and ice via the same processes at act for terrestrial planet fomation. The time scale for giant planet formation in this model hinges on how quickly the core can be assembled and on how rapidly the gas in the envelop can cool and accrete on to the core. In the competing Disk Instability theory, giant planets form promptly via the gravitational fragmentation of an unstable protoplanetary disk. Fragmentation requires that the disk is able to cool on a relatively short time scale (comparable to the orbital time scale).

[1] from http://exoplanet.eu/

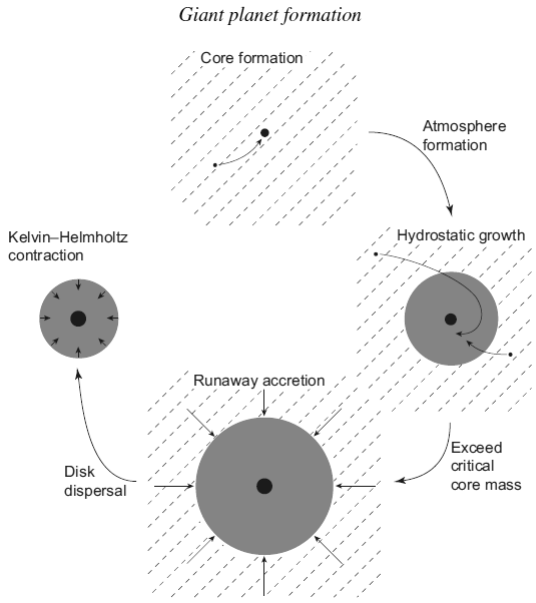

Figure 1: Stages in the formation of giant planets via core accretion.

The following discussion about planets formation mechanism is based on the book "Astrophysics Planet Formation" written by Philip J. Armitage (2010).

1.1.1 Core accretion

The core accretion model for gas giant formation is based on one strong assumption: a seed planet (or core) grows via two-body collisions rapidly enough that it can exceed a certain critical mass prior to the dissipation of the gas disk. If this condition is satisfied, it can be shown (Perri and Cameron, 1974; Mizuno, 1980) that the core triggers a hydrodynamic instability that results in the onset of rapid gas accretion on to the core. Since the critical core mass is typically of the order of 10 $M_{\oplus}$, the end result is a largely gaseous and heavy element enriched planet that at least qualitatively resembles Jupiter or Saturn.

Figure 1 illustrates the four main phases in the formation of giant planets via core accretion:
Core formation: a solid protoplanet core grows via two-body collisions until it becomes massive enough to retain a significant gaseous atmosphere or envelope. The physics during this initial phase is identical to that of terrestrial planet formation with the rate of

growth being controlled by the initial surface density of rocky and icy bodies and by the extent of gravitational focusing.
Hydrostatic growth: initially the envelope surrounding the solid core is in hydrostatic equilibrium. Energy liberated by planetesimals impacting the core, together with gravitational potential energy released as the envelope itself contracts, must be transported through the envelope by radiative diffusion or convection before it is lost to the large gas reservoir of the protoplanetary disk. Over time both the core and the envelope grow until eventually the core exceeds a critical mass. The critical mass is not a constant but rather a computable function of the planetesimal accretion rate and opacity in the envelope.
Runaway growth: once the critical mass is exceeded a runaway phase of gas accretion ensures. The rate of growth is no longer defined by the cooling properties of the envelope, but instead by the hydrodynamic interaction between the growing planet and the disk. For massive planets the bulk of the planetary envelope is accreted during this phase, which is typically rather brief of the order of 10^5yr.
End of accretion: eventually the supply of gas is exhausted, either as a consequence of the dissipation of the entire protoplanetary disk or, more likely, as a consequence of the planet opening up a local gap in the disk. Accretion tails off and the planet begins a long phase of cooling and quasi-hydrostatic contraction.

We can readily estimate some of the masses that characterize the transitions between these phases. The weakest condition that must be satisfied if a planet embedded within a gas disk is to hold on to a bound atmosphere is that the escape speed v_{esc} at the surface of the planet exceeds the sound speed c_s within the gas. A solid body of mass M_p and material density ρ_m has a radius:

$$R_s = (\frac{3}{4\pi}\frac{M_p}{\rho_m})^{(1/3)}$$

and a surface escape speed:

$$v_{esc} = \sqrt{\frac{2GM_p}{R_s}}$$

The sound speed in the protoplanetary disk can be written in terms of the disk thickness (h/r) and Keplerian velocity v_k via:

$$c_s = (\frac{h}{r})v_k$$

Where h is the mean height of the disk and r the mean radius of the disk.

The condition that $v_{esc} > c_s$ can be expressed as:

$$M_p > (\tfrac{3}{32\pi})^{1/2}(\tfrac{h}{r})^3 \tfrac{M_*^{3/2}}{{\rho_m}^{1/2} a^{3/2}}$$

where a is the orbital radius. This mass is very small: substituting numbers appropriate for an icy body at 5AU in a disk around a Solar mass star with $(h/r) = 0.05$ we find that some atmosphere will be present provided that $M_p \sim 5 \times 10^{-4} M_\oplus$. Most of the mass of an envelope with the above density profile lies in a shell close to the surface of the solid core. We can therefore approximate the envelope mass as:

$$M_{env} \approx \tfrac{4}{3}\pi {R_s}^3 \rho_{(R_s)}$$

where $\rho_{(R_s)}$ is the envelope density evaluated at the surface of the core. Substituting for both the density profile and R_s, the condition that the envelope makes up a not negligible fraction of the total mass:

$$M_{env} > \epsilon M_p$$

Where ϵ represents the threshold above which the envelope could be said to be significant.

In light of the rather crude analysis: a protoplanet must grow before it starts to acquire a massive gaseous envelope, and this must occur prior to the dispersal of the protoplanetary disk. If we assume that the maximum protoplanet mass that can be attained prior to disk dispersal is comparable to the isolation mass we can determine for any particular disk model where in the disk planets will grow fast enough to capture envelopes.

Interior to the snowline the isolation mass is smaller than the minimum mass required for envelope capture. In this region it is unlikely that protoplanets will grow fast enough to capture envelopes prior to disk dispersal, and the ultimate outcome of planet formation will instead be terrestrial planets.

At orbital radii beyond the snowline, conversely, the isolation mass exceeds the minimum envelope capture mass. Giant planet formation is much more likely in this case, though it is unclear whether it will result in planets with a modest but still significant envelope (e.g. Uranus and Neptune) or true gas giants whose mass is dominated by the contribution from the envelope.

It is worth emphasizing that although the isolation mass generically increases at the snowline, the critical radius beyond which the giant planet formation may occur does not always coincide with the radius of the snowline. Using a different disk model (or indeed a

more accurate model for when envelope capture begins) one might instead predict a critical radius for giant planet formation that lies either inside or outside the radius of the snowline. The only safe generalization is that envelope capture becomes more likely at larger orbital radii, and detailed calculations (such as those presented by Bodenheimer et al., 2000) are needed before one can decide whether a particular giant planet is or is not likely to have formed in situ at its observed orbital radius.

Unfortunately if we apply the core accretion scenario to understand the formation of outer giant planets of our Solar System, an extremely long time-scale is required for Neptune and Uranus to form a core, which is estimated to be around 10 million years. Since the gas and dust in the protoplanetary disk probably only lasted for a few million years, this poses quite an issue.

Newer accretion models that accounts for planet migration induced by planet disk interactions may be able to account for their formation within a short enough timescale, but this is still a challenging and ambiguous area.

1.1.2 Disk instability

The disk instability model for giant planet formation is based on the assumption that the gaseous protoplanetary disk is massive enough to be subject to instabilities arising from its own self-gravity, and that the outcome of these instabilities is fragmentation into massive planets. The fundamental difference between this scenario and the core accretion model arises from the fact that in the disk instability model the solid component of the disk is a bystander which plays only an indirect role (via its contribution to the opacity) in the process of planet formation.

Historically the earliest discussions of disk instability as a mechanism for planet formation predate any serious work on core accretion (Kuiper, 1951; Cameron, 1978). Despite this long history, computational methods have only relatively recently advanced to the point of being able to reliably assess the viability of the disk instability theory, and much of the recent work in the field is an offshoot of an influential numerical simulation by Boss (1997).

The conditions needed for a protoplanetary gas disk to become unstable to its own self-gravity is that globally the disk mass must satisfy the relation:

$$\frac{M_{disk}}{M_\star} \geq \frac{h}{r},$$

where M_{disk} is the disk mass and $M_\star$ is the star mass.

Locally we can define a parameter:

$$Q \equiv \frac{c_s \Omega}{\pi G \Sigma} < Q_{crit}$$

where Σ is a surface mean density and Ω is the angular velocity of the disk.Q_{crit} is a dimensionless measure of the threshold below which instability sets in. It lies in the range $1 < Q_{crit} < 2$.

If we compare these requirements to observational determinations of protoplanetary disk properties the global condition suggests that widespread gravitational instability (i.e.instability that extends across a large range of disk radii) must be limited to disks at the upper end of the observed range, with masses of around a tenth of the stellar mass. Such massive disks may be commonly present early in the evolution of pre-main-sequence stars (e.g. Eisner et al., 2005).

For a disk around a Solar mass star the local condition can be written in the form:

$$\Sigma \geq 3.8 \times 10^3 (\frac{Q_{crit}}{1.5})^{-1} (\frac{h/r}{0.05}) (\frac{r}{5AU})^{-2} [gcm^{-2}]$$

It is immediately clear that the surface densities required for gravitational instability are large - more than an order of magnitude in excess of the minimum mass Solar Nebula value at 5AU - but such high surface densities are neither observationally excluded nor unreasonable on theoretical grounds. High surface densities are likely at early epochs when the disk accretion rate is large, especially if angular momentum transport within the disk is rather inefficient and these conditions provide the most fertile ground for the development of gravitational disk instabilities.
Assuming for the time being that gravitational instability results in fragmentation, we can estimate the masses of the objects that would be formed. Noting that the most unstable scale in a gravitationally unstable disk is $\lambda \sim 2{c_s}^2/(G\Sigma)$, we expect that fragmentation will result in objects whose characteristic mass is of the order of $M_p \sim \pi \lambda^2 \Sigma$. For a disk around a Solar mass star with $(h/r) = 0.05$ and $Q_{crit} = 1.5$ this characteristic mass is independent of orbital radius and equal to $M_p \approx 8 M_J$, where M_J is the mass of Jupiter.

This estimate is evidently on the high side for Jupiter and for the majority of known extrasolar planets. That said, it does suffice to establish that disk instability could result in the formation of substellar objects (massive planets or brown dwarfs) and it is easy to imagine - given the crude nature of the estimate - that a more sophisticated calculation might yield objects that populate a large fraction of the mass spectrum of gas giant planets.

A disk will become gravitationally unstable if $Q < Q_{crit}$, but satisfying this condition is not sufficient to guarantee that the result of the instability will be fragmentation. The first linearly unstable modes in a gravitationally unstable disk are generally nonaxisymmetric ones, which develop into a pattern of spiral structure which is able to transport angular momentum outward via gravitational torques. The fact that gravitational instabilities within a disk transport angular momentum is critically important, because it implies that self-gravity is able to transport matter inward and thereby tap into the reservoir of free energy available to the system. Dissipation of the accretion energy, in turn, can then act to heat the disk and (by raising Q) mitigate the strength of the instability.

Summarizing the conditions that the disk be both gravitationally unstable (low Q) and vulnerable to fragmentation (short t_{cool}) is difficult. Much the most likely site for successful formation of substellar objects via disk instability is the outer disk - perhaps at radii of 50 to 100 AU - where fragmentation is a plausible outcome of gravitational instability provided that the disk is massive enough at such large distances from the star. Any planets formed via this channel would almost certainly populate the upper end of the planetary mass function.

At smaller radii of 10 AU and less, fragmentation is not possible if the disk cools via radiative diffusion of energy from the mid-plane to the photosphere, but the disk could approach the fragmentation boundary if the efficiency of cooling is almost as great as that allowed by the thermodynamic requirement that the mid-plane should be hotter than the photosphere.

The answer to the original question of whether a planet such as Jupiter can form via disk instability then rests, ultimately, on the highly technical question of how efficiently energy is transported within the protoplanetary disk, and here one might hope for an answer from numerical simulations. Current simulations, unfortunately, yield only a confused picture, with different groups finding variously rapid cooling and consequent fragmentation or somewhat slower cooling and an absence of fragmentation. Further work is needed to elucidate the origin of these disparate results and determine firm bounds on the regions of the disk that are able to fragment.

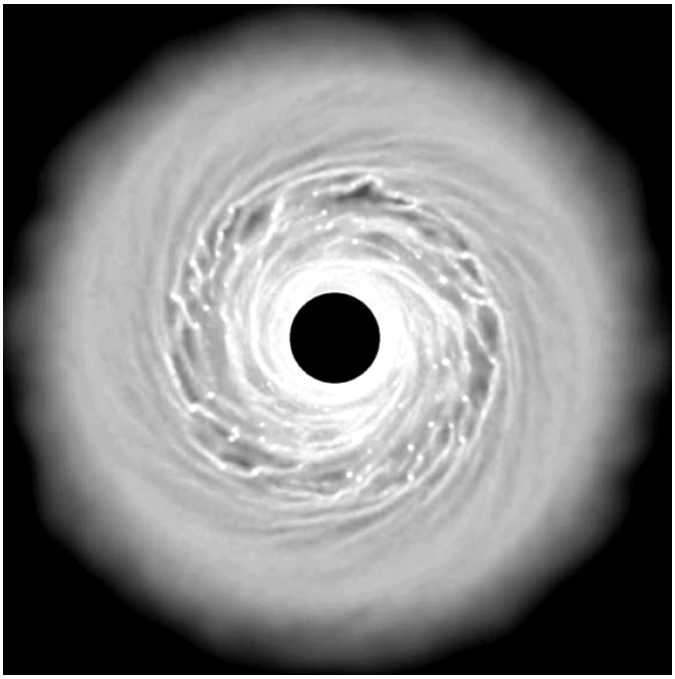

Figure 2: An image of the surface density of a simulated protoplanetary disk that is subject to gravitational instability (Rice et al. 2003). The non-linear outcome of gravitational instability in disks is generally a non-axisymmetric pattern of transient spiral arms. If the cooling time of the gas within the disk is short enough the disk fragments into dense clumps. Provided that these clumps are able to survive and contract further they may form substellar objects (massive planets or brown dwarfs).

1.2 Frequency of planets in wide orbits and distribution of planet parameters

One of the primary goals of extrasolar planets science is a better understanding of the mechanism of formation and evolution of planetary systems. A fundamental observational parameter is the frequency of planets as a function of their mass and the separation from the parent star.

Possibly, the best technique currently available to study the inner side of a planetary system is the radial velocity (RV). RV surveys have already provided a firm determination of the frequency of extrasolar giant planets (size similar to Jupiter or larger) within about 3 AU from the central star (Lineweaver & Grether 2003, Santos et al. 2004, Fischer & Valenti 2005). However, RVs becomes highly inefficient at larger separations, and severe incompleteness will remain for separation larger than 5 AU. The same is true (and even worse) for transits, and in some measure also for microlensing. Direct imaging is then expected to be the most efficient technique, on a short timescale, to discover planets in the outer regions of planetary systems.

As discussed in the previous section the core accretion scenario predicts that the peak of formation of giant planets is expected to close the snowline, thanks to the availability of a larger amount of condensate in the protoplanetary disk. In outer regions the longer timescales involved should make planet formation a less efficient process and therefore it is more likely for the outer regions to be populated thanks to planet-planet interactions or migration mechanisms which alter the original configuration of the system. We then expect to observe a roughly bell-type distribution, which shape is a function of the efficiency of the migration mechanism (that may also create asymmetric distributions or secondary peaks). Furthermore, current models of planet migration within a disk predict smaller migration rates for the most massive giant planets. Therefore, a significant population of massive extrasolar giant planets can be expected not too far from their birth zone (3-10 AU for solar-type stars). According to Ida & Lin (2004) the core accretion mechanism is able to form giant planets up to $\sim$ 30 AU from the central star while outward migration might push some of them up to 50-100 AU from the central star. Depletion of outer disk by photo-evaporation should also favor outward migration.

Formation of planets in-situ at very wide separation might be instead possible for disk instability mechanisms. A further mechanism potentially able to populate the outward regions of a planetary

system is gravitational scattering between planets.

In any case it is clear that, despite of the challenges posed to the models, the formation of giant planets in very wide orbits (e.g. 100 AU) is possible. Therefore a determination of the frequency of giant planets in wide orbits ($>$ 5-10 AU) is key to test several aspects of the planet formation models.

Beside frequency it would also be interesting to derive the distributions of planets parameters such as mass, semi-major axis and eccentricities and any difference with respect to those observed for planets orbiting close to their central star. The details of the mass functions of sub-stellar companions, including brown dwarfs, at wide separation and the study of the existence of the brown dwarf desert will put constraints on their formation mechanisms and the actual mass separation between the two classes of objects.

2 Detecting exoplanets

The current most successful techniques to discover new exoplanets are certainly the radial velocities (RV) and the transits. Radial velocity has been very successful in measuring masses and periods of planets with masses greater than several Earths and in short-period orbits. Transits have been valuable in measuring the diameters and periods of giant planets and in combined-light mode have measured temperature distributions and spectral features. They will also be valuable for determining mass and orbit statistics of distant planets, but its geometric bias precludes using it for the vast majority of nearby systems.

Unfortunately these techniques are focused on the inner ($\leq$ 5AU) region of a planetary system: they are in fact biased towards planets in relatively close orbits and so the orbital separations larger than $\sim$ 5AU are currently not well sampled. Direct imaging surveys, which are typically more sensitive to planets at larger orbital separations, can fill this gap. However a direct detection of exoplanets is technically challenging due to the small angular separation of a very faint source (the planet) from a much brighter one (the host star) and it requires extraordinary efforts in order to overcome the barriers imposed by astrophysics (planet-star contrast), physics (diffraction), and engineering (scattering).

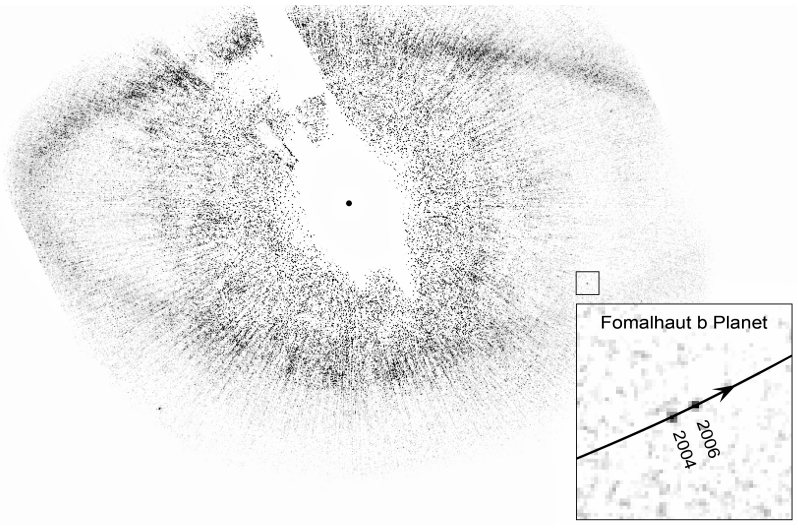

Figure 3: Visible-wavelength image, from the Hubble Space Telescope, of the exoplanet Fomalhaut b. The planet is located just inside a large dust ring that surrounds the central star. Fomalhaut has been blocked and subtracted to the maximum degree possible (Kalas et al. 2008).

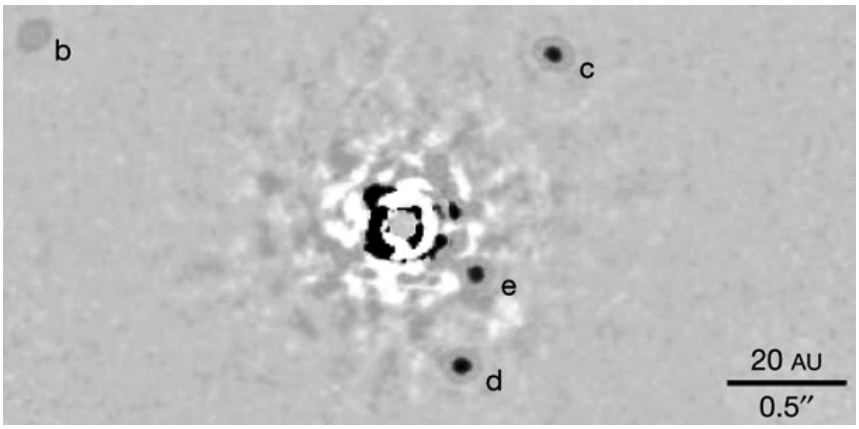

Figure 4: Images of HR8799 (a star at 39.4 ± 1.0pc and located in the Pegasus constellation) were acquired at the Keck II telescope with the Angular Differential Imaging technique (ADI) to allow a stable quasi-static point spread function (PSF) while leaving the field-of-view to rotate with time while tracking the star in the sky. Planets b, c, d and e are seen at projected separations of 68, 38, 24 and 14,5 AU from the central star, consistent with roughly circular orbits at inclinations of < 40 degrees (Marois et al. 2008).

2.1 Direct Imaging of Exoplanets

A direct image of an exoplanet system is a snapshot of the planets and disk around a central star. We can estimate the orbit of a planet from a time series of images and we can evaluate the size, temperature, atmospheric gases, surface properties, rotation rate, and likelihood of life on a planet from its photometry, colors, and spectra in the visible and infrared. The issue here is not the lack of photons from the planet: the exoplanets around stars in the solar neighborhood are expected to be bright enough for us to characterize them with direct imaging; however, they are much fainter than their parent star, and separated by very small angles. Viewed from a ground-based telescope, with a star-planet separation of less than 1 arcsec (Jupiter viewed from 5 pc) the planet signal is immersed in the photon noise of the telescope's diffraction profile ($\lambda/D \simeq 0.02$ arcsec at 1500nm for a 8m telescope) and more problematically within the "seeing" profile (of order 1 arcsec) arising from turbulent atmospheric refraction. Under these conditions elementary signal-to-noise calculations imply that obtaining a direct image of the planet is not feasible. The conventional imaging techniques are then totally inadequate and new methods are needed. These methods are directed at reducing the angular size of the stellar image, suppressing scattered light (including use of coronographic masks), minimising the effects of atmospheric turbulence (including eliminating them

altogether using space observations), and enhancing the contrast between the planet and the star by observing at longer wavelengths for detection of thermal emission (Perryman, 2000).

Adaptive optics has been under intensive development for the latest generation of large astronomical telescopes, aiming to compensate for atmospheric phase fluctuations across the telescope pupil in order to achieve diffraction-limited resolution. The method relies on a continuous measurement of the wavefront from a reference star and the subsequent application of an equal but opposite correction using a deformable mirror containing actuators distributed across its surface, at frequencies of the order of 1 kHz.

Adaptive systems typically rely on a nearby bright reference star to measure these phase fluctuations. Measurements must be made within a narrow coherent region, the isoplanatic patch, and over pupil sub-apertures of size $\simeq r_0$, where r_0 is the atmospheric coherence length ($0.15 - 0.2$m at a good site at visible wavelengths, increasing to ~ 1m at 2μm).

The use of artificial laser guide stars from resonant scattering in the mesospheric sodium layer at ~ 95km extends the applicability of the technique to arbitrary locations on the sky. However, due to the different light path, the corrections obtained though artificial laser stars are less accurate than those provided by natural guide star and cannot be used in high contrast imaging.

From the imaging point of view the detectable planets can be roughly divided into three classes: hot Jupiters, young and self-luminous planets and mature exoplanet.

Hot Jupiters have not yet been directly imaged, but their large thermal flux, 10^{-3} to 10^{-4} times the parent star, means that they will likely be imaged in the future. Their extreme closeness to the parent star requires extreme angular resolution, so the images will come from long-baseline interferometers, not from single-dish telescopes.

Young and self-luminous planets are the only ones to be directly imaged, because their high temperature and large size give them a strong, detectable flux, and their large distances from their parent stars makes them easier to see in the halo of atmospherically or instrumentally scattered star light. These young and self-luminous planets are likely to continue to be prime targets for the direct-imaging technique in the near future, owing to this combination of favourable parameters.

Giant planets at young ages are mostly self luminous and their luminosity depending on age, mass and atmosphere composition. They are much more luminous in the near infrared than in the visible domain, with peaks of emission around wavelengths 1.05, 1.25, 1.6

and 2.1 μ depending on their effective temperature. To understand why they have this property we should consider the early evolution of massive planets.

After a bright and short accretion phase, contraction and differentiation are the remaining energy sources of the planet. Initially, the planet is still quite warm ($T \sim 1500K$) and bright (about 100 times brighter than Jupiter). However, young planets cool off in a few tens of millions of years, so they will be found only around young stars, and not around nearby (older) stars. Lacking dynamical informations, mass estimates for young planets depend strongly on the assumed system age, planetary atmosphere models, and initial thermodynamic state, leading to large uncertainties in the inferred mass. Planetary mass estimates conventionally assume a "hot start", in which the planet is initially in a high-temperature and a high-entropy (and hence, luminous) state (Baraffe et al. 2003; Burrows et al. 1997). However, recent theoretical models suggest that giant planets produced according to standard formation theories could initially be much colder (Marley et al. 2007; Fortney et al. 2008; Spiegel&Burrows 2012). In this work, young and self-luminous planets are our candidates.

Finally a mature exoplanet may be defined here as one with an effective temperature that is roughly comparable to its star-planet equilibrium temperature. At old ages, the intrinsic flux of planets becomes small and thus their contrast strongly depends on the distance and on reflective properties of the atmosphere: albedo and polarization level. These planets, like those in the solar system or around mature nearby stars, will be fainter in the infrared than young, self-luminous planets, and therefore will require more sophisticated techniques to image them (Seager S., 2010). Their detection is generally beyound what is possible with 8m telescope, while they will be amoung the most interesting targets for future telescope such as the E-ELT.

The number of planets detected by direct imaging is currently still low, only 65[2] detections. However, already these discoveries, like the planets around HR 8799 (Marois et al. 2008) or β Pictoris (Lagrange et al. 2010) have triggered numerous theoretical studies regarding their formation (e.g., Dodson-Robinson et al. 2009; Kratter et al. 2010).

Two points about these young and self-luminous planets are interesting: their large semi-major axis and the fact that we directly measure the intrinsic luminosity at young ages in several IR bands.

[2]http://exoplanet.eu/

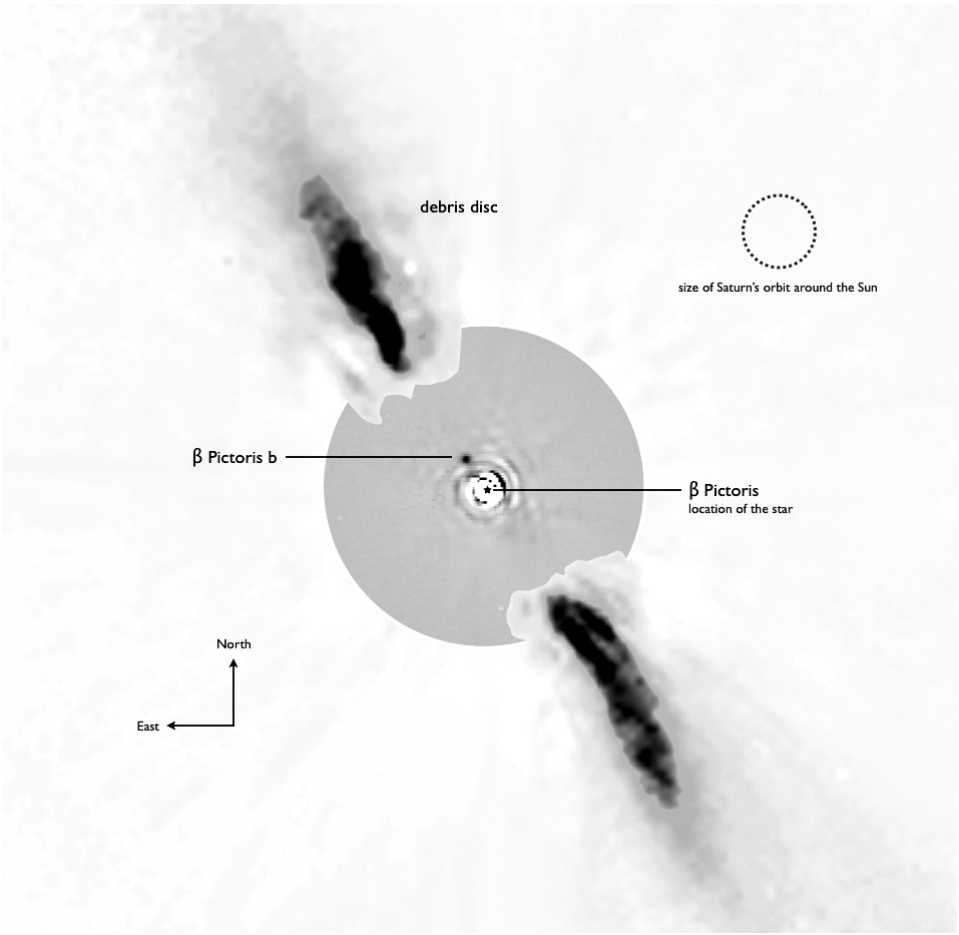

Figure 5: This composite image represents the close environment of Beta Pictoris as seen in near infrared light. This very faint environment is revealed after a very careful subtraction of the much brighter stellar halo. The outer part of the image shows the reflected light on the dust disc, as observed in 1996 with the ADONIS instrument on ESO's 3.6 m telescope; the inner part is the innermost part of the system, as seen at 3.6 microns with NACO on the Very Large Telescope. The newly detected source is more than 1000 times fainter than Beta Pictoris, aligned with the disc, at a projected distance of 8 times the Earth-Sun distance. Both parts of the image were obtained on ESO telescopes equipped with adaptive optics (Lagrange et al. 2008).

Both quantities are important to understand the formation mechanism (core accretion or disk instability) and in particular the physics of the accretion shock occurring when the accreting gas hits the planet's surface during formation (Commercon et al. 2011). If the gravitational potential energy of the accreting gas is radiated away, low entropy gas is incorporated into the planet, leading to a faint luminosity and small radius (so-called "cold start", Marley et al. 2007) while the accretion of high entropy material leads to a "hot start" with a high luminosity and large radius (e.g., Burrows et al. 1997; Baraffe et al. 2003).

2.2 SPHERE

SPHERE (Spectro Polarimetric High contrast Exoplanet Research) is the new high contrast imager for the VLT, in operation since spring 2014. The prime objective of SPHERE is the discovery and study of new extra-solar giant planets orbiting nearby stars by direct imaging of their circumstellar environment. The challenge consists in the very large contrast between the host star and the planet, larger than 12.5 magnitudes (or 10^5 in flux ratio), at very small angular separations, typically inside the seeing halo. The whole design of SPHERE is optimized towards reaching the highest contrast in a limited field of view and at short distances from the central star. Both evolved and young planetary systems are detectable, respectively through their reflected light (mostly by visible differential polarimetry) and through the intrinsic planet emission (using IR differential imaging and integral field spectroscopy).

The following discussion about SPHERE is based on the article: SPHERE a "Planet Finder" instrument for the VLT written by Beuzit J.L et al, 2008.

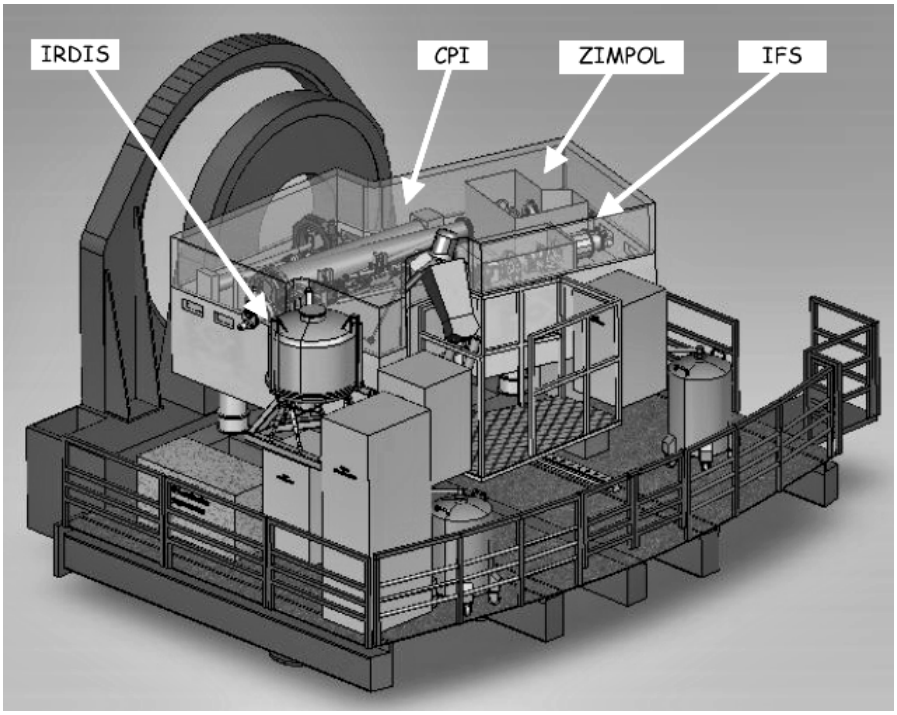

Figure 6: Schematic view of SPHERE on the Nasmyth platform.

The design of SPHERE is divided into four subsystems: the Common Path and Infrastructure (CPI) and the three science channels, a

differential imaging camera (IRDIS, InfraRed Dual Imaging Spectrograph), an Integral Field Spectrograph (IFS) and a visible imaging polarimeter (ZIMPOL, Zurich Imaging Polarimeter).

The Common Path includes pupil stabilizing fore optics (tip-tilt and rotation), calibration units, the SAXO extreme adaptive optics system, and NIR and visible coronagraphic devices. ZIMPOL shares the visible channel with the wavefront sensor through a beamsplitter, which can be a grey (80% to ZIMPOL) beamsplitter, a dichroic beamsplitter, or a mirror (no ZIMPOL observations). IRDIS is the main science channel responsible for wide-field imaging in one or two simultaneous spectral bands or two orthogonal polarizations and low and medium resolution long slit spectroscopy. The IFS, working from 0.95 to 1.65 μm, provides low spectral resolution (R$\sim$30) over a limited, 1.8"$\times$1.8", field-of-view.
A photon sharing scheme has been agreed between IRDIS and IFS, allowing IFS to exploit the NIR range up to the J band, leaving the H band, judged optimal for the DBI mode, for IRDIS for the main observation mode. This multiplexing optimizes the observational efficiency.

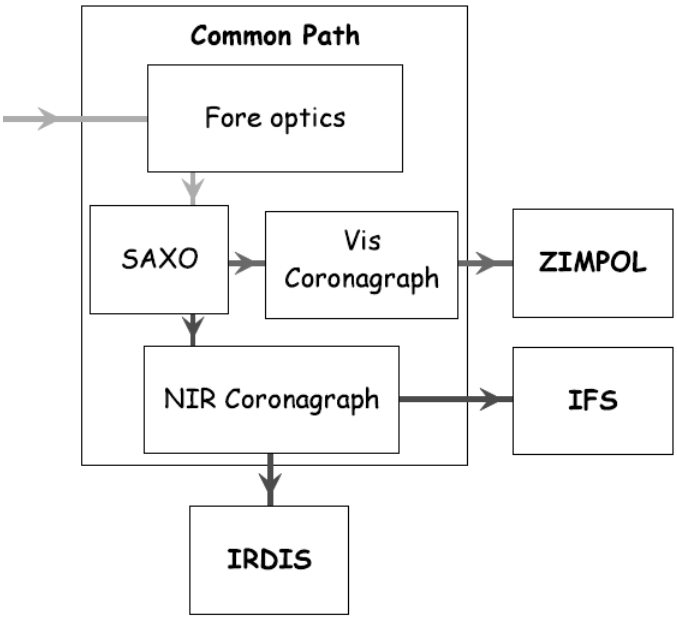

Figure 7: SPHERE sub-systems including the common path (CPI) with adaptive optics system SAXO, coronagraphs, and sub-instruments IRDIS, IFS and ZIMPOL.

2.2.1 Common Path and Infrastructure (CPI)

The common path is mounted on a large actively damped optical bench to which each science instrument dock as a whole. SPHERE is entirely enclosed in a thermal/dust cover and includes a comprehensive automated cryo-vacuum system supplying 4 cryostats and a separate vacuum container.

Besides classical optical components, the common path embeds numerous new high-technology components like a high order deformable mirror from CILAS, toroidal mirrors manufactured by spherical polishing of pre-stressed substrates1, a dedicated electron multiplying CCD for wavefront sensing, achromatic 4 quadrants coronagraph, classical and apodized Lyot coronagraphs. A good number of these components have one or more of their degrees of freedom motorized, for a total of around 60 motors.

Extreme adaptive optics (SAXO)

Three loops and one off line calibration compose the SAXO extreme adaptive optics system.

The main AO loop corrects for atmospheric, telescope and common path defects. The main impact is the increase of detection signal to noise ratio through the reduction of the smooth PSF halo due to turbulence effects.

The Differential Tip-Tilt loop ensures a fine centering of the beam on the coronagraphic mask (correction of differential tip-tilt between VIS and IR channel). It will therefore ensure an optimal performance of the coronagraph device.

The Pupil Tip-Tilt loop corrects for pupil shift (telescope and instrument). It ensures that the uncorrected instrumental aberrations effects (in the focal plane) is always be located at the same position and thus is canceled out by a clever post-processing procedure.

Non-Common Path Aberrations are measured with phase diversity, and their pre-compensation will lead to the reduction of persistent speckle.

The 41×41 actuator High Order DM of 180 mm diameter displays a best flat of 5nm rms surface and maximum stroke $>\pm 3.5$ μm.

The wavefront sensor is a 40×40 lenslet Shack-Hartmann, covering the 0.45-0.95μm spectral range, and equipped with a focal plane spatial filter continuously variable in size from λ/d to $3\lambda/d$ at 0.7 μm, where d is the sub-aperture diameter, for aliasing control.

At the heart of the AO system is a Real Time Computer (RTC) called SPARTA: Standard Platform for Adaptive optics Real Time Applications, the new generation RTC from ESO, providing a global AO loop delay $<$1 ms. SPARTA allows to control the 3 system loops

but it also provide turbulent parameters and system performance estimation as well all the relevant data for an optimized PSF reconstruction and a clever signal extraction from scientific data.

Coronagraphs

Coronagraphy is key for reaching our science goals. Its action is to reduce by a factor $\geq$100 the intensity of the stellar peak, and to eliminate the diffraction features due to the pupil edges.

The baseline coronagraph suite includes an achromatic four-quadrant phase mask coronagraph (A4Q) based on precision mounting of four half-wave plates (HWP), and both a classical Lyot coronagraph (CLC) and an apodized Lyot coronagraph (ALC). In the J and Y bands the nulling performance is decreased with a peak-to-peak attenuation of 350 and 315 respectively. However, contrast levels are quite homogeneous with respect to the H band, another indication of reasonable achromatization.

While the CLC option, with mask diameter of about $10\lambda/D$, is within the realm of classical manufacturing, the ALC option requires an apodizer in the coronagraph entrance pupil.

2.2.2 InfraRed Dual Imaging Spectrograph (IRDIS)

The IRDIS science module covers a spectral range from 0.95 - 2.32 μm with an image scale of 12.25 mas consistent with Nyquist sampling at 950 nm. The FOV is 11"$\times$12.5", both for direct and dual imaging. Dual band imaging (DBI) is the main mode of IRDIS, providing images in two neighboring spectral channels with $<$10 nm rms differential aberrations.

Two parallel images are projected onto the same 2k$\times$2k detector with 18μm square pixels, of which they occupy about half the available area. A series of filter couples is defined corresponding to different spectral features in modeled exoplanet spectra. The classical imaging (CI) mode allows high-resolution coronagraphic imaging of the circumstellar environment through broad, medium and narrow-band filters throughout the NIR bands including Ks.

In addition to these modes, long-slit spectroscopy (LSS) at resolving powers of 50 and 500 is provided, as well as a dual polarimetric imaging (DPI) mode.

A pupil-imaging mode for system diagnosis is also implemented.

All these modes require a coronagraph in the common path system and a corresponding Lyot stop in the IRDIS Lyot stop wheel. For the Long Slit Spectroscopy mode, the coronagraph mask is replaced by a coronagraphic slit. The slit is centered on the star, which

is covered by a central patch, and a disperser device equipped with a dedicated Lyot stop is located in the IRDIS Lyot stop wheel. Two dispersion devices are provided, a double prism for low resolution (LRS, ∼50) and a grism for medium resolution (MRS, ∼500). The prism can be used with either a YJHKs filter or a YJH filter, and the grism is used only with the YJH filter.

The main challenge of IRDIS is to achieve less than 10 nm differential aberrations between the two channels. An error budget based on high-quality polishing technology satisfies the requirement.

The beam-splitter option has been favored over the Wollaston option because it eliminates spectral blurring problems, which would limit the useful FOV, and allows the use of high-quality materials with high homogeneity.

Dual-band imaging performance

Numerical simulations of the IRDIS performance have been made using the SPHERE CAOS module (a numerical simulation tool for astronomical adaptive optics). These model results have been fully confirmed by the on-sky performances. For this mode, the Top Level Requirement is a contrast of 5×10^{-5} at 0.1" and 5×10^{-6} at 0.5" from the star in 1-hour integrations achieved by imagery at both sides of the H-band methane absorption edge. High contrast imaging has to deal at first order, with two components: a speckled halo which is averaging over time and a static speckle pattern originating from quasi-static aberrations evolving occurring with a much longer lifetime than atmospheric residuals. Because the DBI mode is performing simultaneous differential imaging, performances are mostly limited by the quasi-static aberrations upstream the coronagraph and by the spectral separation between DBI filters.

2.2.3 Integral Field Spectrograph (IFS)

IFS are very versatile instruments, well adapted for spectroscopic differential imaging as needed for detection of planets around nearby stars. The main advantage of IFS is that differential aberrations can be kept at a very low level; this is true in particular for lenslet based systems, where the optical paths of light of different wavelength within the IFS itself can be extremely close to each other. Additionally, IFS provide wide flexibility in the selection of the wavelength channels for differential imaging, and the possibility to perform spectral subtraction, which in principle allows recovering full information on the planet spectra, and not simply the residual of channel subtraction, as in classical differential imagers.

The main drawback of IFS is that they require a large number of detector pixels, resulting in a limitation in the field of view, which is more severe for lenslet-based systems. Classical differential imagers and IFS are then clearly complementary in their properties, and an instrument where both these science modules are available may be extremely powerful for planet search.

Both a classical TIGER and an innovative BIGRE concept have been considered for the SPHERE IFS, the latter being finally selected because of its better properties. Both these designs are based on lenslet systems: in the case of TIGER design the array of micropupil images created by the lenslet array are imaged on the detector, after having being dispersed; in the case of the BIGRE array, a second lenslet array allows formation of pseudo-slit images corresponding to a very small portion of the field, which are then imaged on the detector after being dispersed. The main advantage of the BIGRE concept is that the pseudo-slit images are only very mildly dependent on wavelength and have a quasi-top-hat profile, while in the TIGRE concept the micropupil images are diffraction images with secondary maxima, whose size is dependent not only on wavelength, but also on the illumination of the individual lenslets. The BIGRE system allows a better control of diffraction effects and a much lower level of cross-talk.

Optimized commonality between IFS and IRDIS in terms of detector and associated equipment is seen as an important system goal. The same 2k×2k detector format is therefore adopted, and the long-wavelength cut off defined for IRDIS is also acceptable for IFS.

In addition to the micro-lens system at the entrance of the spectrograph, the opto-mechanical concept includes collimation optics, an Amici Prism providing zero beam deviation and constant resolution within the entire wavelength range, camera optics, and the detector cryostat. Thermal background is controlled by extending the cryostat >150mm in front of the detector, thus limiting the solid angular view of the warm environment, and by including a cold short-pass filter.

Detector dithering (in order to improve flat-field precision) is achieved by small movements of the camera optics, realized by commercial piezo's.

2.2.4 Zurich Imaging Polarimeter (ZIMPOL)

ZIMPOL is located behind SPHERE visible coronagraph. Among its main specifications are a bandwidth of 600-900 nm and an instantaneous field of view of 3×3 arcsec (C. Petit et al., 2008), with

access to a total field of view of 8" diameter by an internal field selector.

The ZIMPOL optical train contains a common optical path that is split with the aid of a polarizing beamsplitter in two optical arms. Each arm has its own detector. The common path contains common components for both arms like calibration components, filters, a rotatable half wave plate and a ferroelectric liquid crystal polarization modulator. The two arms have the ability to measure simultaneously the two complementary polarization states in the same or in distinct filters.

The images on both ZIMPOL detectors are Nyquist sampled at 600 nm.

The detectors are both located in the same cryostat and cooled to 193,15K. The rest of the ZIMPOL opto-mechanical system is at ambient temperature.

The basic ZIMPOL principle for high-precision polarization measurements includes a fast polarization modulator with a modulation frequency in the kHz range, combined with an imaging photometer that demodulates the intensity signal in synchronism with the polarization modulation. The polarization modulator and the associated polarizer convert the degree-of-polarization signal into a fractional modulation of the intensity signal, which is measured in a demodulating detector system by a differential intensity measurement between the two modulator states. Each active pixel measures both the high and the low states of the intensity modulation and dividing the differential signal by the average signal eliminates essentially all gain changes, notably changes of atmospheric transparency or electronic gain drifts.

For the SPHERE implementation, the modulator is a ferroelectric liquid crystal working at a frequency of about 1 kHz. The demodulator is a special CCD camera, which measures for each active pixel the intensity difference between the two modulation states. For achieving this, every second row of the CCD is masked so that charge packages created in the unmasked row during one half of the modulation cycle are shifted for the second half of the cycle to the next masked row, which is used as temporary buffer storage (the CCD is equipped with cylindrical micro-lenses which focus the light onto the open CCD rows). After many thousands of modulation periods the CCD is read out in less than one second.

The sum of the two images is proportional to the intensity while the normalized difference is the polarization degree of one Stokes component. Because the measurement is fully differential, systematic error sources are reduced to a very low level (on the order 10^{-5}).

The main requirement is that the incoming signal is not strongly polarized ($p < 10^{-2}$).

3 The SHINE Survey

In May 2014 the VLT's new generation planet imager SPHERE successfully achieved first light. As described in the previous Chapter, SPHERE provides accurate exoplanet detection performance owing to a combination of high-order XAO (extreme adaptive optics) correction, coronography, and differential imaging. These capabilities enable the detection of faint planets at small angular separations from bright stars. The SHINE program is a component of the Guaranteed Time Observations (GTO) that the SPHERE Consortium has received in exchange of the massive investments in manpower and cash. The SHINE survey is a large near-infrared survey of $400 - 600$ young, nearby stars. The survey started in Febrary 2015. Up to now, about 60 observing nights were dedicated to SHINE with about 130 scientific targets observed.

3.1 Survey goals

The main scientific goals of SHINE are to characterize known planetary systems (architecture, orbit, stability, luminosity, atmosphere) and to search for new planetary systems using SPHERE's unprecedented performance.
In particular the SHINE Science Goals are:

- Determine the frequency of giant planets beyond 5 AU;
- Investigate the impact of stellar mass on the frequency and characteristics of planetary companions over the range 0.5 to 3.0 $M_{\odot}$;
- Study the architecture of planetary systems (multiplicity and dynamical interactions);
- Investigate the link between the presence of planets and disks (in synergy with the GTO program aimed at disk characterization);
- Identify a broad set of new planetary companions and provide a first order planet characterization.

3.2 Stellar sample

The target list for the SHINE survey include 400 stars and ~ 40 special targets selected from a compilation of 1200 stars including the following classes of targets:

- Nearby young associations (10-100 Myr, 30-100pc) will offer the best chance of detecting low mass planets, since they will have brighter sub-stellar companions.
- Young active F-K dwarfs of the Solar neighbourhood (ages less than 1 Gyr, $d < 50pc$).
- Nearest stars (all ages within 20pc of the Sun) will allow probing the smallest orbits and will also be the only opportunities for detecting planets by directly reflected light.
- Young early type stars especially the members of the Sco-Cen region (d $\sim$ 140pc, age $11 - 17$Myr)

A figure of merit was constructed for each individual target taking in consideration apparent magnitude, distance, age and spectral type. The highest figure of merit is attributed to those targets that have the highest probability of hosting a planet detectable by SPHERE according to power-law models. Two different models were considered and the final figure of merit is a combination of them.

The stars are grouped in 4 priority groups according to the following selection criteria:

- P_1: important targets and young/moving groups members (120 stars).
  - P_1+: additional 40 Sco-Cen members (early-type with $M \geq 1.5M_\odot$) and 40 field stars (solar and low-mass with $M \leq 1.5M_\odot$) selected according to a figure of merit.
    Total of 200 stars.
- P_2: 20 stars from young/moving groups, 40 Sco-Cen members and 120 field stars selected according to the figure of merit for early-type with $M \geq 1,5M_\odot$ and solar/low-mass with $M \leq 1.5M_\odot$.
  Total of 200 stars.
- P_3 and P_4: 40 Sco-Cen members and again field stars selected according to the figure of merit for early-type with $M \geq 1.5M_\odot$ and solar/low-mass with $M \leq 1.5M_\odot$.

The 4 groups mentioned above form the sample to be used for the statistical analysis (hereafter the statistical sample). The figure of merit does not include information on already detected planets by various techniques, presence of disks, etc. In this way, it is suitable for an unbiased determination of planet frequency.

Two additional groups were defined:

- P0: special targets that include star with known planets and brown dwarf detected by imaging and stars with disks signatures, suggesting the presence of planets.
- P_5: Bad weather filler.

Some of special targets are included in the statistical sample independent of the reason for upgrading them to special targets and they are kept on the sample for the statistical analysis.

3.3 Results of the first year of observations

In this work we will use the data from the first two semesters of the SHINE survey. Within this time, 88 objects, that are part of the statistical sample, were successfully observed with IFS (Integral-Field-Spectrograph) leading to 12 candidates of which 4 were confirmed so far. Since we expect that the probability that candidates indeed reveals as faint companions is deemed low, hereinafter we will only consider confirmed objects in our discussion.

The Fig.8 shows the distribution of stellar masses in the observed sample in $M_\odot$. They cover the range of $[0.5 - 3]M_\odot$ with a median value of 1.22 $M_\odot$.

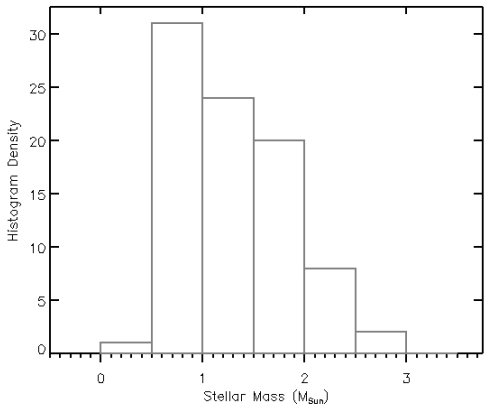

Figure 8: Distribution of stellar masses.

The distribution of stellar age in our sample (in *gigayear*) is shown in the Fig.9. The observed stars are in a range of $1 - 500$Myr with a median value of 30 Myrs .

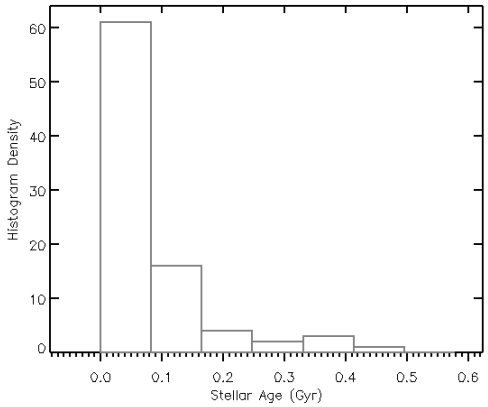

Figure 9: Distribution of stellar ages.

The distribution of stellar distances in our sample (in *parsec*) is shown in Fig.10. They are within 170 pc with a mediam value of 48.2 pc.

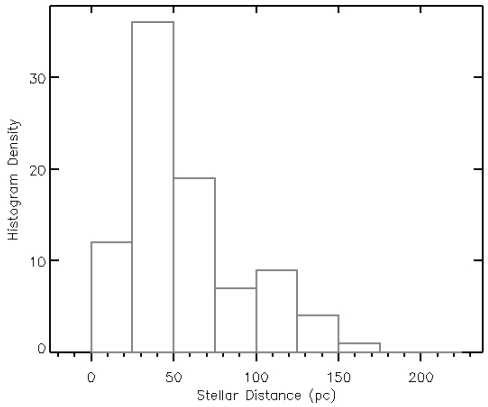

Figure 10: Distribution of stellar distances.

In this thesis we consider data obtained with IFS (integral field spectrograph). IFS is expected to be the most sensitive instrument to detect planet at separation <0.8 arsec from the star. For a median star in our sample (distance of 48.2 pc) they correspond to a projected separation of 39 AU.

The priority selection has arranged 16 targets in P0, with 11 of them upgraded from P1 to P0, 55 in P1 and finally 17 P2. In the Figure 11 we present the number of target observed versus the target priority.

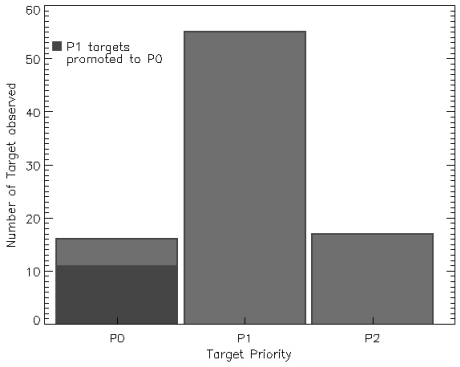

Figure 11: Distribution of targets priorities.

The reason for an upgrade from a initial-priority selection to a final-priority selection is mainly due to a previous knowledge of the existence of the companion from other survey. This upgrade must then be taken into account in the statistical discussion. We will discuss this point later.

3.3.1 Detection limits

Our analysis is based on confirmed detections and detection limits. These last one were obtained for each individual targets at the end of a very complex procedure based on differential imaging that includes injecting recovery of artificial planets obtained by properly scaling the PSF. A description of the details of this procedure is beyond the purpose of the present discussion. The reader may refer to Zurlo et al. (2015). The detection limits of the instrument expressed in ΔMag in J band versus projected-separation in AU for all the targets in the survey are given in Fig. 12 on the following page. For separations larger than 0.3 arsec, ΔMag is tipically larger than 12 mag with a median value of $\sim$ 14mag. In best cases the limiting magnitude is as good as 16 mag. These contrasts are at least 2-3 magnitudes deeper than typically achieved in previous similar surveys (e.g. Chauvin et al. 2015) thanks to the excellent performances of SPHERE. For this reason, we expect that the SHINE survey may lead to more strigent constraints on the properties of planetary systems.

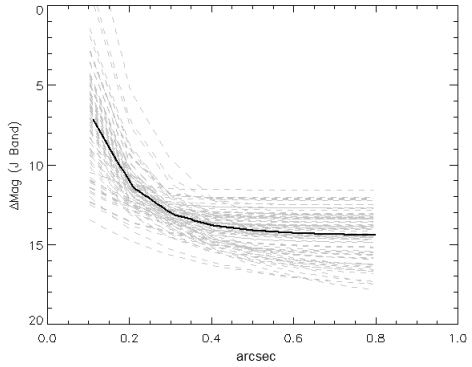

Figure 12: Detection limits in magnitudes (in the J-band) for all targets of the survey (dashed lines). The thick solid line is the median value at each separation.

We transformed the detection limits in magnitudes at different separation (in arcsec) from the star into detection limits in mass at different projected separations (in AU).

We used here the COND Model by Baraffe et al. (2003) which assumes the so called hot-start scenario. We note here that there are various models of planet evolution which provide quite different predictions about their luminosity in the J-band in particular at very young ages. We prefer to use the hot start model because they better agree with observational constraints the the case of βPicb (Bonnefoy et al. 2014) and of the the planets of HR8799 (see e.g. the discussion in Esposito et al. 2013).

The detection limits of the instrument expressed in minimun-detectable-mass (in M_J) versus projected-separation (in AU) are shown on the left panel of the Fig. 13. The right panel of this figure summarizes the statistical weight corresponding to the limits shown on the left panel. To this purpose in this picture we show contour plots corresponding to the number of targets for which we have information (that is, for which we are above the detection limit) in the projected separation vs mass plane. From this figure, it is clear that for a large fraction of the SHINE targets, we are sensitive to planets with masses $> 5M_J$ over the separation range 10-40 AU. The lack of sensitivity at larger separations is simply due to the limited field of view of the IFS and to the typical distance of the SHINE targets. The complementary IRDIS data (not discussed in this thesis but available in the SHINE survey) would allow to extend the sensitivity of the survey up to about 200 AU for most targets. On the other hand the lack of sensitivity at small separations is due to the starlight glare; while SPHERE is order of magnitudes better

than previous generation high-contrast imager, still does not allow to explore at high-contrast the regions very close to the stars.

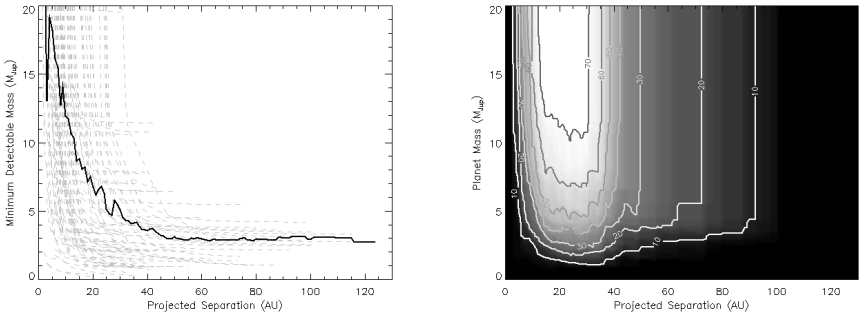

(a) *Detection limits in mass M_J as a function of separation for SHINE targets.*

(b) *Contour plots showing the number of targets for which we have information (that is, above the detection limit) as a function of projected separation and planet mass.*

Figure 13

3.3.2 Detections

The detection limits discussed so far should be compared to the actual confirmed detection. Four planet-mass objects around three stars were detected on the IFS SHINE data and a few additional ones on IRDIS data. Images of these planets obtained with IFS are shown in Figure 14. Actually, these are not new discoveries.

β Pic b was discovered by Lagrange et al. (2008) from NACO data; the planets around HR8799 were found by Marois (2008, 2010) using Keck data; and 51 Eri b was discovered by B. Macintosh (2015) using GPI data. However, the stars around which these planets were found were included in our target list independently of the fact that they were known to host planets, and they would have been detected by SPHERE even if no previous observations of them were available. They can then be considered as SHINE detections for our statistical analysis.

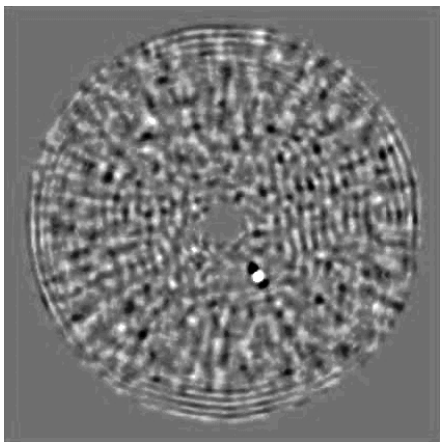

(a) *β Pic b*

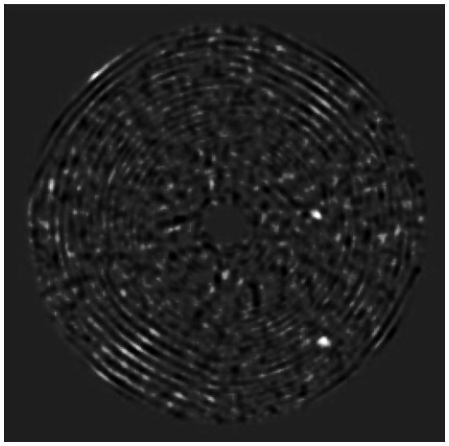

(b) *HR 8799d and HR 8799e*

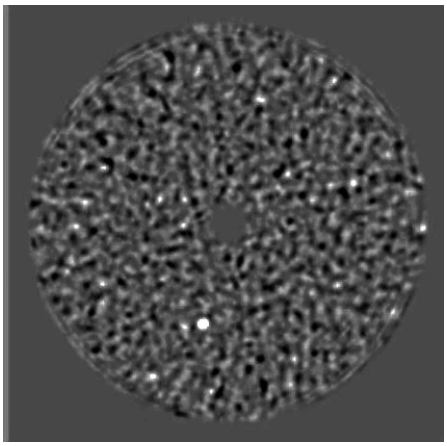

(c) *51 Eri b*

Figure 14

The main properties[3] of these four planets are detailed in Table1.

Table 1: Confirmed detections

Name	Mass (M_J)	Semi-major axis (AU)	Initial-Prority	Final-Priority
β Pic b	$7.0(^{+4.0}_{-3.0})$	13.18(±0.09)	$P1$	$P0$
51 Eri b	7.0(±5.0)	$14.0(^{+7.0}_{-3.0})$	$P1$	$P0$
HR8799 d	10.0(±3.0)	27.0	$P1$	$P0$
HR8799 e	9.0(±4.0)	14.5(±0.5)	$P1$	$P0$

[3]Mass and Semi-major axis from http://exoplanet.eu/

3.3.3 Number of detections

In this work, although the total detections represent a key data, a fundamental information for a rigorous statistical analysis is the *weight* of a detections.

The weight of a detection of a companion to a target placed in a priority P0 depends on the fact that the objects of a priority P0 are more likely to be observed than those with priority P1.

We estimated the weight to be given to a detection for an object that had an upgrade from P1 to P0 as follows:

N_1 is the number of objects with priority P1 and n_1 the number of P1 objects observed. The probability that a target with priority P1 is observed is therefore $p_1 = n_1/N_1$.

N_0 is the number of objects P0 and n_0 the number of P0 objects observed. The probability that a target with priority P0 is observed is then $p_0 = n_0/N_0$.

The weight w given to a target that has been upgraded from P1 to P0 is the ratio between p_1 and p_0:

$$w = p_1/p_0 = \frac{(n_1/N_1)}{(n_0/N_0)}$$

In particular, for our detections, we have the following upgrades:

Name	Initial-Prority	Final-Priority
β Pic b	$P1$	$P0$
51 Eri b	$P1$	$P0$
HR8799 d	$P1$	$P0$
HR8799 e	$P1$	$P0$

The number of objects in P1 and P0 and the number of objects observed in P1 and P0 are:

$N_1 = 184$ number of objects in P1; $n_1 = 55$ number of objects observed in P1;
$N_0 = 48$ number of objects in P0; $n_0 = 16$ number of objects observed in P0;

The final *weight* of each detections is then 0.9.

The total number of the detection is 3 (not *weighed*); we in fact remind that the detection of more companions in a planetary system are evaluated in our analysis as a single detection, i.e HR8799d and HR8799e.

The *weighed detections* are then 2.7.

The fraction of the planets is therefore 3.07%. It corresponds to the percentage of the *weighed detections* $(3 \times 0,9)$ of the over total number of the observed targets (88).

4 Statistical Analysis

Over the past years, several groups (Kasper et al. 2007; Lafreniére et al. 2008; Chauvin et al. 2010; Nielsen & Close 2010, Nielsen et al. 2013, Biller et al. 2013, Brandt et al. 2014, Clanton et al. 2015) initiated statistical analyses to constrain the physical and orbital properties (mass, period, eccentricity distributions) of the giant planet population at large separations. These groups developed statistical analysis tools appropriate for exploiting the performances of deep imaging surveys. They also tested the consistency of various sets of parametric distributions of planet properties, using the specific case of a null-detection. The first assumption of these tools is that planet mass and period distributions coming from the statistical results of radial velocity (RV) studies at short period (Cumming et al. 2008) can be extrapolated and normalized to obtain information on more distant planets. Despite the model dependency on the mass predictions, the approach is attractive for exploiting the complete set of detection performances of the survey and characterizing the outer portions of exoplanetary systems.

In this chapter we introduce an overview on the estimation of the planet frequency, its statistical formalism and the statistical code to estimate the probability that such a planet companion would be detected from our observations.

4.1 Estimation of the planet frequency

Previous studies, although with different samples and sensitivities, converge towards a similar conclusion: the frequency of planets above $2-4M_J$ around F-M stars is below $\sim 10-20\%$ beyond $\sim 50AU$ at high-confidence level. They have used their non-detections to investigate with what confidence planet distributions obtained from RV surveys (Cumming et al. 2008) can be extrapolated for planets at much larger orbital radii.

In the following sections, we present the statistical formalism and finally we introduce the code Quick-MESS, developed by Bonavita et al. (2013), used to perform the analysis of the our data.

4.1.1 Statistical formalism

Our formalism for the statistical analysis is based on previous works by Carson et al. (2006) and Lafreniére et al. (2007). We consider the observation of N stars enumerated by $j = 1 \ldots N$. We call f the fraction of stars that have at least one companion of mass

and semi-major axis in the interval $[m_{\min}, m_{\max}] \cap [a_{\min}, a_{\max}]$, and p_j the probability that such a companion would be detected from our observations.

With these notations, the probability of detecting such a companion around star j is (fp_j) and the probability of not detecting it is $(1 - fp_j)$.

Denoting $\{d_j\}$ the detections made by the observations, such that d_j equals 1 if at least one companion is detected around star j and 0 otherwise.

The likelihood of the data given f is

$$L(\{d_j\}|f) = \prod_{j=1}^{N} (1 - fp_j)^{1-d_j} \cdot (fp_j)^{d_j} \tag{1}$$

The determination of the probability that the fraction of stars having at least one companion is f is obtained from Bayes' theorem:

$$p(f|\{d_j\}) = \frac{L(\{d_j\}|f) \cdot p(f)}{\int_0^1 L(\{d_j\}|f) \cdot p(f) df}, \tag{2}$$

where $p(f)$ is the a priori probability density of f, or prior distribution, and $p(f|\{d_j\})$ is the probability density of f given the observations $\{d_j\}$, or posterior distribution.

Since we have no a priori knowledge of the wide-orbit massive planets frequency, we adopt a "maximum ignorance" prior: $p(f) = 1$. Given a confidence level (CL) α, we can use the posterior distribution $p(f|\{d_j\})$ to determine a confidence interval (CI) for f using

$$\alpha = \int_{f_{\min}}^{f_{\max}} p(f|\{d_j\}) df, \tag{3}$$

where $f_{\min}$ and $f_{\max}$ represent the bounding values of f, i.e. the minimal and maximal fraction of stars with at least one planetary companion. Following Lafreniére et al. (2007), an equal-tail CI $[f_{\min}, f_{\max}]$ is found by solving:

$$\frac{1-\alpha}{2} = \int_{f_{\max}}^{1} p(f|\{d_j\}) df \tag{4}$$

$$\frac{1-\alpha}{2} = \int_{0}^{f_{\min}} p(f|\{d_j\}) df \tag{5}$$

Again, when a value of α is fixed, Eq. 4 and 5 become implicit equations on $f_{\min}$ and $f_{\max}$ that can be solved numerically.

The critical step of this statistical analysis is the determination of p_j, the completeness, for all observed targets. This completeness represents the fraction of companions that would have been detected in the interval $[m_{\min}, m_{\max}] \cap [a_{\min}, a_{\max}]$. It is directly related to the sensitivity of the observations to the physical parameters of the planets, which in turn is a function of the detection limits, age and distance of each star.

To estimate p_j in this analysis we use the Quick-MESS code.

4.1.2 Quick-MESS

Quick-MESS is a novel way to perform statistical analyses of direct imaging surveys where the standard Monte Carlo approach is replaced by grid-based sampling of the orbital parameters, which leads to a substantial reduction in the required computational time. It uses the information on the instrument performances to assess for each target the probability that a planet of a given mass and semi-major axis can be detected. In the Quick-MESS code the standard Monte Carlo approach is replaced by grid-based sampling of the orbital parameters, which leads to a substantial reduction in the required computational time. The main out put of the code is the probability of detecting a planet in the considered parameter space, given a set of assumptions on the distribution of the planet orbital parameter and the mass-luminosity function.

The steps of the code are the following:

1. Evaluate the distribution of planets with a certain normalised separation, s, as a function of the orbital parameters and integrate and normalise it to get f(s, e): the distribution of planets as a function of the eccentricity e and the normalized separation s, where s is defined as $s = R/a$ with R the physical separation and a the planet's semi-majoraxis.

2. Multiply $f(s, e)$ for the eccentricity distribution $f(e)$

3. Use the planetary evolutionary models (e.g Baraffe et al. 2003) to estimate, for each target in the studied sample, the minimum detectable planetary mass M_{lim} as a function of the projected separation (ρ), given the contrast limits of the instrument.

4. For each value of semi-major axis on an uniform grid, use the distance of the star to convert the normalised separation s into the physical projected separation ρ, thus obtaining $f(\rho, e)$ from $f(s, e)$.

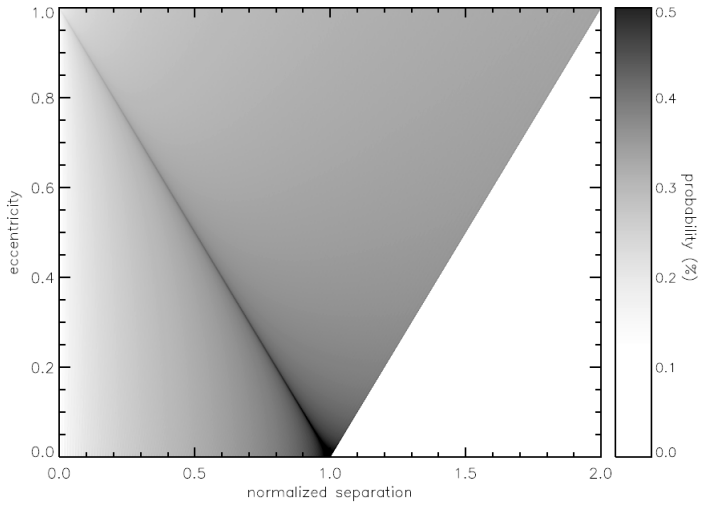

Figure 15: Projection probability, as a function of the eccentricity and normalised separation (Bonavita et al. 2013).

5. For each value of the planetary mass (M_p) over an uniform grid find the range of projected separations where $M_P > M_{lim}$ and integrate $f(\rho, e)$ over this interval to obtain the distribution of detectable planets with a given value of mass and semi-major axis $f(M_p, a)$

6. Finally multiply $f(M_p, a)$ with the required mass and semi-major axis distributions ($f(M_p)$ and $f(a)$, respectively) to obtain the detection probability map $g(M_p, a) = f(M_p, a)f(M_p)f(a)$

7. In the case of a survey, integrate $F(M_p, a)$ over the whole range of masses and semi-major axis, in order to obtain $p(M_{min} \leq M_p \leq M_{max}, a_{min} \leq a \leq a_{max})$ the probability of detecting a planet in the considered parameter space.

Evaluation of the projection probability The distribution of planets - given a certain combination of orbital parameters - that can be found at a certain position on their projected orbit is assessed by calculating the orbit of the planet in normalized separation $s(\phi) = R(\phi)/a$, (where a is the semi-major axis of the orbit, and R is the radius vector that, together with the true anomaly ν, gives the polar coordinates of the planet on the orbit).

In this way we construct $f(s, e, \omega, i)$ as the distribution of planets found at a given separation, where e is eccentricity, ω is the argument

of periastron and i is the inclination of the orbit.

Since ω and i are assumed to be uniformly distributed, they can be integrated over in order to give $f(s, e)$: the distribution of planets with a given normalised separation and eccentricity:

$$f(s, e) = \int_0^{2\pi} \int_0^1 f(s, e, \omega, cosi)\, d\omega\, dcosi$$

$f(s, e)$ represents the fraction of planets with a certain combination of eccentricity e and normalised separation s; therefore we will refer to it as projection probability.

Calculating the detection probability The projection probability $f(s, e)$ is necessary to evaluate the probability of finding a planet of mass M_p and separation a, which is the final goal of QMESS. Together with $f(s, e)$ a set of distributions for the planet eccentricity ($f(e) = dN/de$),mass ($f(M_p) = dN/dM_p$) and semi-major axis ($f(a) = dN/da$) is also needed.

The next step consists in converting the instrument detection limit (expressed in minimum planet/star contrast detectable in the chosen band for a given target, as a function of the projected separation ρ) into a minimum planet mass (M_{lim}) vs projected separation limit. To do this, a set of mass-luminosity models are used (e.g. Baraffe et al. 2003; Burrows et al. 2003), assuming that the planet and the star are coeval.

Subsequently, the code generates an uniform grid of masses, $M_{min} < M_p < M_{max}$, and semi-major axes, $a_{min} < a < a_{max}$, and evaluates the distribution of detectable planets $f(M_p, a)$. First, for each semi-major axis we use the distance d of the star to evaluate the projected separation $\rho = sa/d$ and obtain $f(\rho, e)$ for each value of a on the grid. Then for each value of M_p the values of ρ_{min} and ρ_{max} are evaluated from the detection limits, such as $M_p \leq M_{lim}$ for $\rho_{min} \leq \rho \leq \rho_{max}$.

$f(M_p, a)$, defined as the distribution of detectable planets as a function of M_p and a, is then calculated as:

$$f(M_p, a) = \int_0^1 \int_{\rho_{min}(M_p,a)}^{\rho_{max}(M_p,a)} f(\rho, e)\, d\rho\, de$$

The limits on ρ (ρ_{min} and ρ_{max}) are defined by the minimum and maximum separation at which a planet is detectable given the contrast curve.

The (expected) distribution for semi-major axes $f(a)$ and planet mass $f(M_p)$ - all normalised - are then folded into the $f(M_p, a)$ to provide:

$$g(M_p, a) = f(M_p, a) f(a) f(M_p)$$

a new distribution of detectable planets, now taking into account the observed/predicted distribution of planets. $f(M_p, a)$ and $g(M_p, a)$, as well as $f(s, e)$ represent the fraction of detectable planets with a given mass, M_p, and semi-major axis, a, assuming $f(a)$ and $f(M_p)$ as the distributions of those parameters.
Finally $g(M_p, a)$ is integrated over the considered range of mass and semi-major axis to obtain the probability of detecting a planet with $M_{min} \leq M_p \leq M_{max}$ and $a_{min} \leq a \leq a_{max}$:

$$p(M_{min} \leq M_p \leq M_{max}, a_{min} \leq a \leq a_{max}) = \int_{M_{min}}^{M_{max}} \int_{a_{min}}^{a_{max}} g(M_p, a)\, dM_p\, da$$

p can be also used to evaluate the upper/lower limits on the frequency of planets in the range of mass and semi-major axis explored by the analysed survey for a given set of assumptions on the mass and semi-major axis distributions.

5 Results of statistical analysis

5.1 Testing the planet parameters distribution

An interesting aspect of our sample is the possibility to place some initial constraints on the distributions of mass and semimajor axis for the giant planet population.

5.1.1 Planet parameter distribution

The approach taken by previous studies was to try extrapolating at large separations the distributions coming from RV surveys, which are usually parameterized with power laws. One of the most complete RV study on this topic for FGKM stars is the one performed by Cumming et al. (2008) using the sensitivity limits from the Keck Planet Search. They determine that the planet frequency for solar-types stars is 10.5% for $0.3 - 10 M_J$ planets over the separation range $0.3 - 2.5$AU and that the mass and semimajor axis distributions are best modeled with power laws respectively of index $\alpha = -1.31$ and $\beta = -0.61$, i.e. $dN \propto M^{-1.31} dM$ and $dN \propto a^{-0.61} da$.

Very recently a similar analysis have presented by Brian et al. (2016) based on a large and updated sample, extending at large periods. These two analysis are the comparison basis for our discussion.

For our study we assume the frequency of the planets f is known over a certain range of mass and semi-major axis from RV surveys, and we model the mass and semimajor axis distributions as power laws. To obtain meaningful results it is important to define the range of mass and semimajor axis over which the frequency f is known and valid. The ranges of values of our analysis that include the masses and the semimajor axis of our data are $[5, 15] M_J$ and $[5, 80]$ AU. The range is different from that of Cumming et al. use of their relation for our separation range clearly represents an extrapolation. Clearly, we cannot extrapolate the power law dependencies obtained at small separation to arbitrary large values, since this would give an infinite number of planets around each star. A cutoff on the semimajor axis distribution (a_{cutoff}), with a step of 20 AU in the range of $20 - 80$ AU, is then introduced to define an upper limit to the separation. This procedure is similar to that adopted in previous studies (see e.g. Nielsen and Close 2010). Assuming such a form for the distribution is clearly unphysical and as we will see, it leads to result in contradiction with observations. It shall then only be considered as an attempt to fit a more complex distribution with a minimum of free parameters.

Since, our observations are not sensitive to the same range of mass and semimajor axis as the RV data, so the value of f needs to be normalized to be valid inside the range of parameters where we are sensitive, $[m_{min}, m_{max}]$ for the planet mass and $[a_{min}, a_{max}]$ for the semimajor axis.

We notice that the expected fraction of planets F per star is:

$$F = C_o \int_{M_{min}}^{M_{max}} M^{\alpha}\, dM \int_{1}^{a_{cutoff}} a^{\beta}\, da \tag{6}$$

Here M is the planet mass, a the semimajor axis and C_o is the normalization constant defined in such a way that:

$$F = C_o \int_{1M_J}^{13M_J} \int_{0.3AU}^{2.5AU} M^{\alpha} a^{\beta}\, dM\, da = 0.0394$$

that is the value given by Cumming et al. for this mass and semimajor axis range. This normalization ensures that the new frequency, f', is valid over $[m_{min}, m_{max}]$ and $[a_{min}, a_{max}]$, and that its value over $[1, 13]M_J$ and $[0.3, 2.5]$AU is always equal f to match the RV data.

Finally, assuming N_{obs} is the number of observed detection and N_p is the number of expected detections, we use Poisson statistics to obtain the probability that this expected number of detections matches our real detections:

$$P\left(N_{obs}, N_p\right) = \frac{{N_{obs}}^{(N_p)}}{N_p!} e^{(-N_{obs})}$$

5.1.2 Comparison with Q-Mess results

Once detection limits and number of detections in our sample are defined, we may use the Q-Mess code to estimate the expected number of detections in our sample given an assumed distribution of planet frequencies. In our approach, the distribution is defined by three parameters (α, β, a_{cutoff}). By repeating this exercise for a large number of values covering a wide grid, we may discuss what is the range of these parameters that is compatible with the observed number of detections in our sample.

We can visualize the space of expected-planet-detection as a three-dimensional space where the three coordinate axes are α, β and a_{cutoff}. In this way, the iso-expected-planet-detection surface in a 3D space (α, β, a_{cutoff}) is represented in a 2D space (α, β) by a line, the iso-expected-planet-detection line for various specific semi-major axes cut-off.

In Fig.16 and 17 we present the expected fraction of systems with planet detections estimated using Q-Mess (left panel) compared with the actual detection fraction and the corresponding contour plots of the confidence level on the right panel.

In Fig.16 we show this comparison fixing the power law index in mass α $(-1.3, 0.0, 1.3)$. In Fig.17 we show the same but this time fixing the power law index in semi-major axis β $(-0.6, 0.0, 0.6)$. The range of the fixed indexes were selected to bracket the indexes of Cumming et al. (2008) ($\alpha = -1.31$ and $\beta = -0.65$). The red line, in the left panels of both figures, is our observed fraction of detected planet (3.07%).

We remind that increasing the value of α is equivalent to increasing the proportion of high-mass planets and that increasing the value of β is equivalent to increasing the proportion of planets at large orbital separations.

The contour plots shown on the right panel of Fig.15 and 16 display the confidence level with which we can exclude different combinations of parameters α and β in our range of $[5, 15]M_J$ and of $[5, 80]$ AU for a given cut-off value.

In fig.18, we display the results obtained by cutting the (α, β, a_{cutoff}) space for three values of the semi-major axis cut-off (20, 40 and 80 AU). The three panels of this figure show the expected fraction of systems with detected planets as a function of the power law index α for the mass and the power law index β for the orbital separations. The star symbol corresponds to the values reported by Cumming et al. (2008): $\alpha = -1.31, \beta = -0.65$.

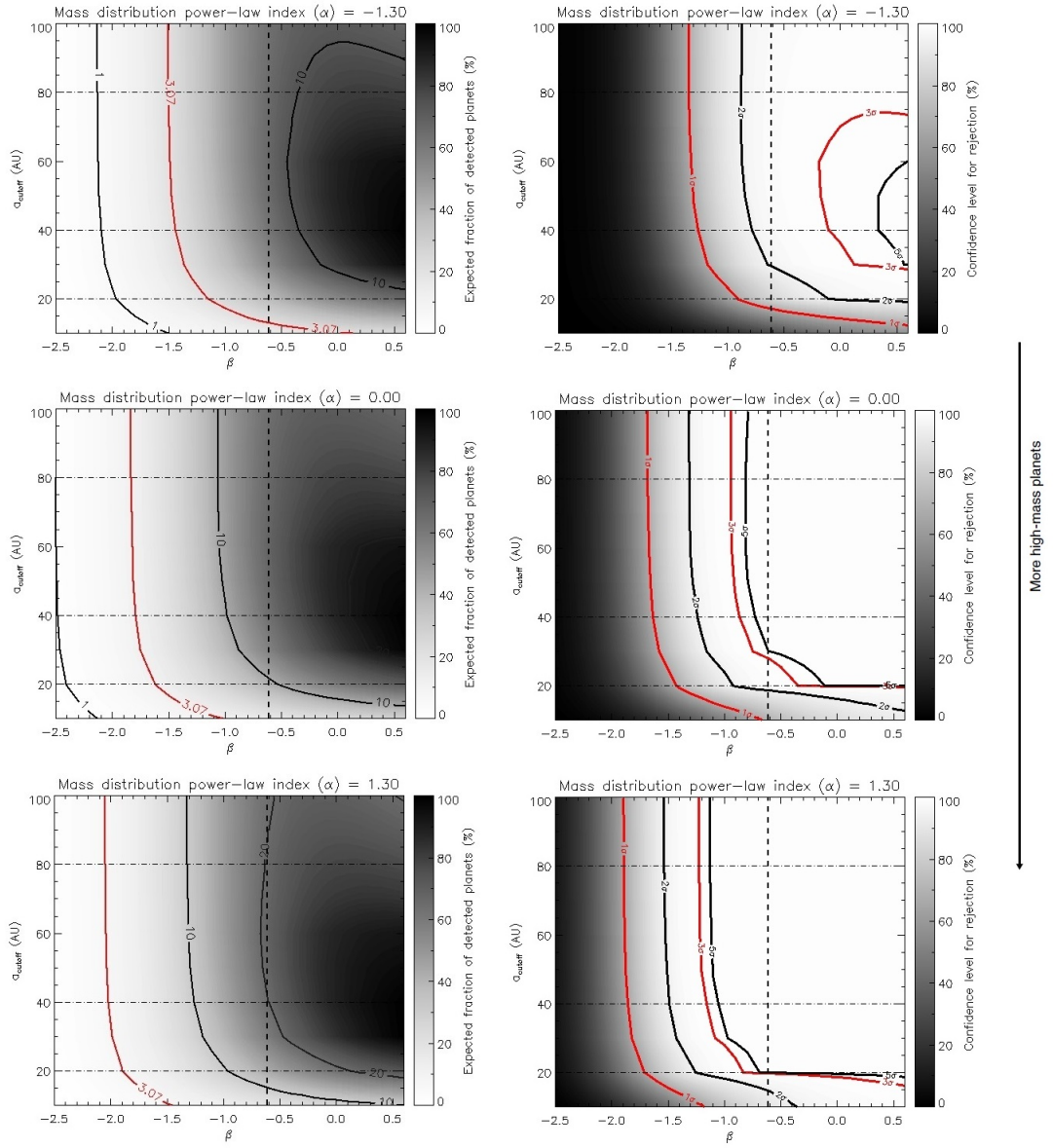

Figure 16: In the left panel the expected fraction of detected planets as a function of the power-law index β of the semimajor axis and of the semi-major axis distribution cut-off, where the mass power-law index α is fixed at -1.3, 0.0 and 1.3 respectively. In the right panel the contour plots show the confidence level where we include (or exclude) the Cumming's values. The curves are for confidence levels of 1σ, 2σ, 3σ and 5σ. The mass range considered is $5 \leq M_p \leq 13 M_J$. The dotted line corresponds to $\beta = -0.61$(Cumming et al. 2008).

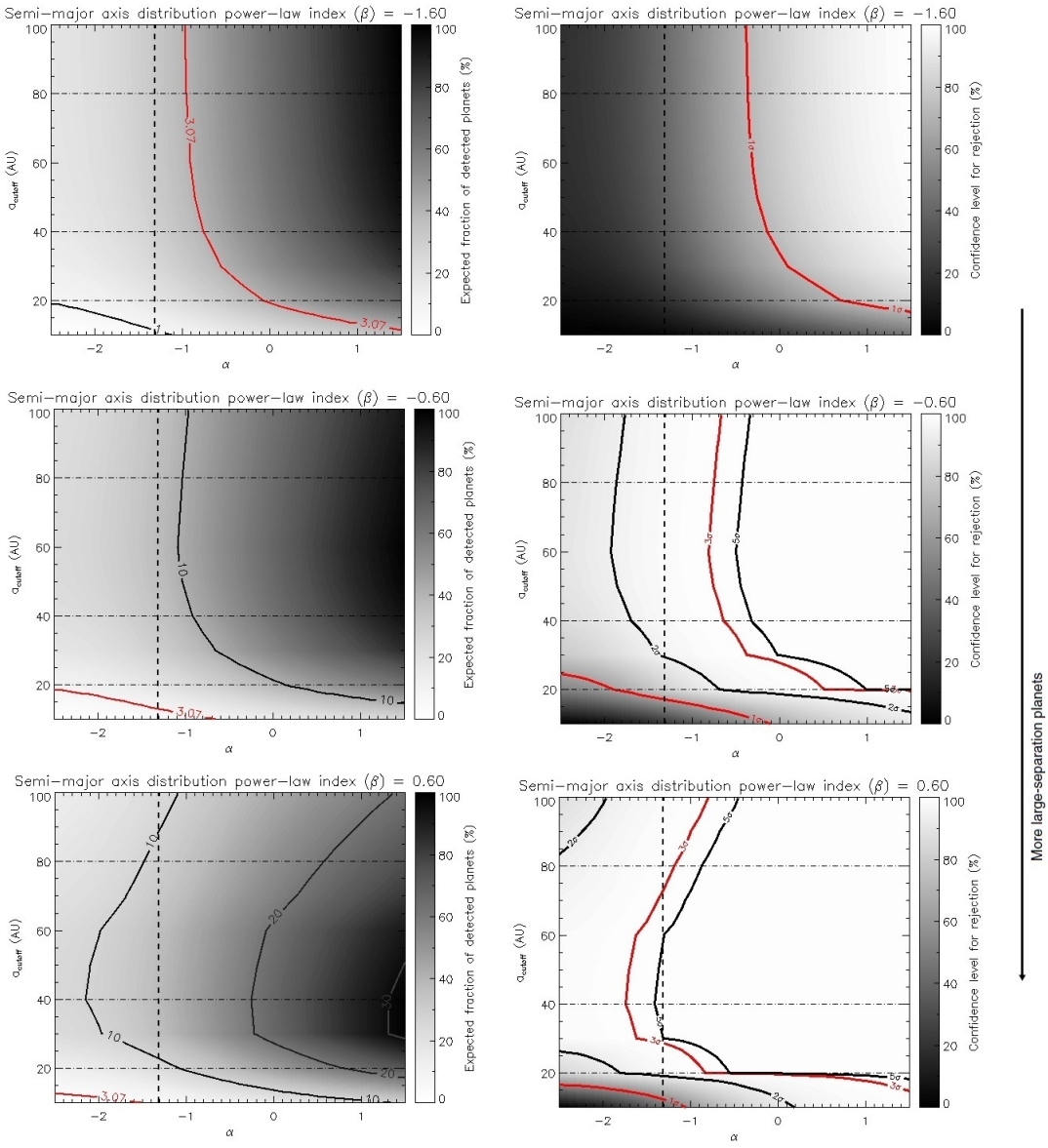

Figure 17: In the left panel the expected fraction of detected planets as a function of the mass power-law index α and of the semi-major axis distribution cut-off, where the power-law index β of the semimajor axis is fixed at -1.6, -0.6 and 0.6 respectively. In the right panel the contour plots show the confidence level where we include (or exclude) the Cumming's values with a confidence level of 1σ, 2σ, 3σ and 5σ. The mass range considered is $1 \leq M_p \leq 13 M_J$. The dotted line corresponds to $\alpha = -1,31$ (Cumming et al. 2008).

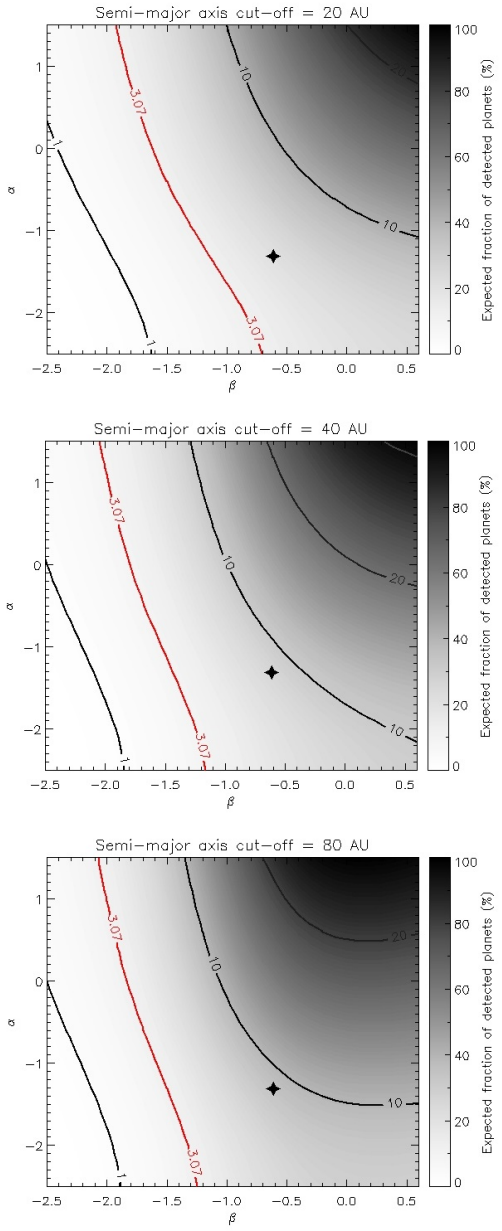

Figure 18: Expected fraction of detected planets as a function of the power law index α for the mass and the power law index β for the semi-major axis distributions for different cut-off (a_{max}) values (20, 40 and 80 AU). The star is the value of α and β distributions from Cumming et al. (2008) $\alpha = -1.31$ and $\beta = -0.65$.

5.2 Clues on the frequency of giant planets in wide orbit

In this section we estimate the frequency of exoplanetary systems in a mass interval of $[5-15]M_J$ for three semimajor axis intervals: $[5-20]$AU, $[5-50]$AU and $[5-100]$AU.

For each targets in our sample, the individual target detection limits allows to estimate (using Q-Mess) the probability p_j that a planet is detected around that star. We may then evaluate the mean of this values over the whole survey over the $[5-15]M_J$ range and for the three semimajor axis intervals defined above. The values of p_j for each target is then also used in Eq.(1) to calculate the likelihood for values of f between 0 and 1.

Using numerical integration of the likelihood with respect to f, the posterior distribution $p(f|dj)$, where d_j are the detections, is derived using Eq. (2). The posterior distribution is obtained assuming a linear-flat prior for the frequency and a flat mass distribution for the planets.

A linear-flat distribution represents an important hypothesis: all masses (in our range of $[5-15]M_J$) at all semimajor axes (in our interval of $[5-20]$AU, $[5-40]$AU and $[5-80]$AU) are assumed to be equally probable.

Finally, 95% and 68% confidence intervals are calculated using numerical integrations of Eqs. (4) and (5).

We present in the three panels of Fig.19 the probability density function of f calculated from our observations for the different ranges of separation. We estimate the planetary systems frequency around the whole stellar sample to be $7.5^{+6.6}_{-2.3}$% for the interval $[5-20]$AU, $6.9^{+6.2}_{-2.1}$% for the interval $[5-50]$AU and $8.9^{+8.0}_{-2.7}$% for the interval $[5-100]$AU at a confidence level of 68% (1σ). This is the frequency of planets with mass $> 5M_J$ consistent with our detections. We remind that these values relie on the assumption made in the Q-MESS code that the mass and semimajor axis distributions of the planets are flat.

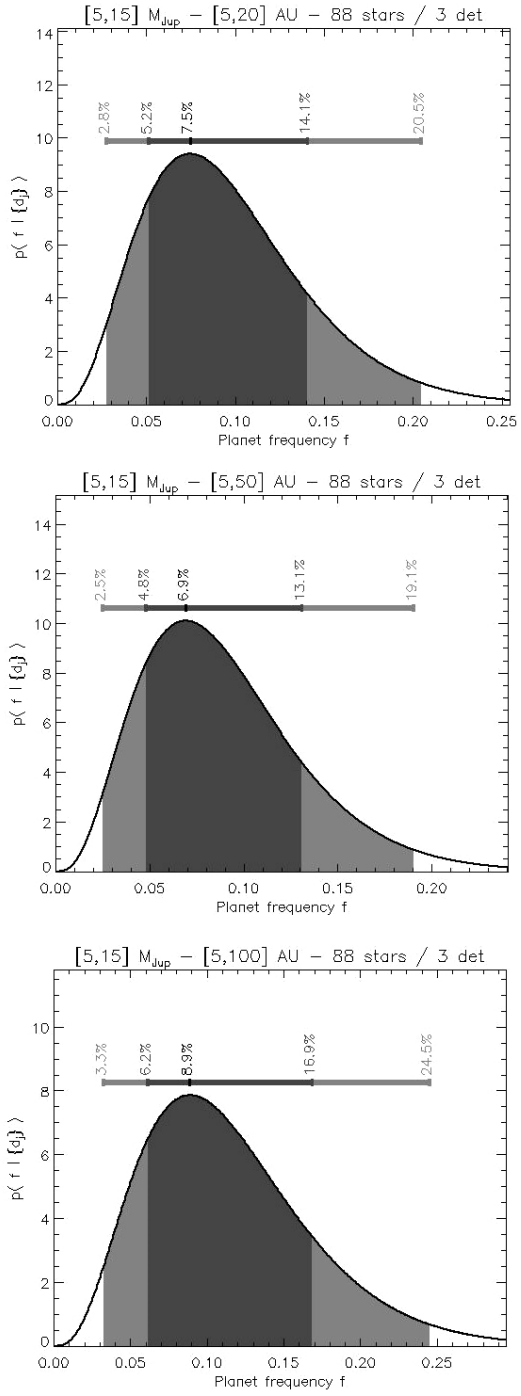

Figure 19: Representation of the probability density of f given the observations d_j (posterior distribution) as a function of the planetary systems frequency f, in three semimajor axis intervals [5-20] AU, [5-50] AU and [5-100] AU and a mass interval $[5-15]M_J$.

6 Discussion of the results

6.1 Comparison with previous direct imaging surveys

Over the past years, a significant number of deep imaging surveys have been reported in the literature, dedicated to the search for exoplanets around young, nearby stars (Chauvin et al. 2003; Lowrance et al. 2005; Masciadri et al. 2005; Biller et al. 2007; Kasper et al. 2007; Lafreniere et al. 2007, Nielsen et al. 2013, Biller et al. 2013, Brandt et al. 2014, Clanton et al. 2015).

Various instruments and telescopes were used with different imaging techniques (coronagraphy, angular or spectral differential imaging) and observing strategies. Several potential planetary mass companions were discovered by these survey; however sometime these companions are at large physical separations, suggesting they formed through a mechanisms possible different with respect to the inner part of system.

The general idea is then to try to construct on overall view of planet distribution over a wide range of separations, connecting results at small separations (from RV surveys) with more at large separations (from direct imaging surveys). Since results from RV surveys are typically given as power-law distributions, the results from direct imaging surveys are compared with extrapolation of these power-laws at large separations. Obviously it's a big challenge to investigate in a semi-major axis interval away from the small "safe zone" given by RV survey.

We consider here two among the most recent works. Nielsen& Close (2010) considered results from the VLT NACO H and Ks band planet search, the VLT and MMT Simultaneous Differential Imaging (SDI) survey and the Gemini Deep Planet Survey. A total of 118 targets were used to set constraints on the population of giant extrasolar planets. They proposed a model for extrasolar giant planets with power-laws for mass and semi-major axis as in Cumming et al. (2008). They concluded that the cut-off semi-major axis is ≤ 65 AU with 95% confidence.

Reggiani et al. (2016) used the results of the NACO-LP (Chauvin et al. 2015, Desidera et al 2015). This database contains 84 objects with a similar selection to these of the SHINE survey. In their statistical analysis Reggiani et al. only considered a subset made of 57 FGK stars with null-detection in the planetary regime and four detections in the brown dwarfs (BD) regime. They modeled the population of substellar objects as the sum of a massive component (BD) and of a less massive one (planets). For this last, they used

a Cumming-like distribution and let the cut-off separation as a free parameter. For what concern the planet distribution (that was not the main focus of their discussion) they concluded that a cut-off radius < 100 AU is in agreement with observations. A further analysis considering the whole NACO-LP sample is in preparation (Vigan et al. 2015).

6.2 Comparison with radial velocity surveys

In this discussion we compare our results with two principal works: Cumming et al. (2008) and Bryan et al. (2016).

6.2.1 Comparison with Cumming et al. (2008)

Cumming et al. (2008) presented the first extensive analysis of the distribution of planets detected from RV surveys. Their main results was to show that over the range of mass and separations that they considered, the frequencies of planets increase with the separation and decrease with the mass. More in details, they show that the distributions of giant planets may be described by a double power law with the planet mass and semimajor-axis with indexes of α and β. The range of separation is close to the parent star: $0.5 - 2.5$ AU and the range of planet masses is $1 - 13\ M_J$.

In order to compare theirs with our results, the first two plots (top of the panel) of Fig.16 we have fixed the Cumming's value of the index ($\alpha = -1.3$). In this way, we are analysing the expected-fraction of systems with detected planets as a function of the index β versus the distribution of semi-major axes cut-off.

The iso-expected-fraction line of our detected planets (red line) crosses the the Cumming's value of the index $\beta = 0.6$ at ~ 10 AU. We can accept the Cumming's value of the index $\beta = 0.6$, with a confidence level of 1σ, up to 15 AU as semimajor-axis cutoff. For a cut-off of 20 AU we need to adopt a value of $\beta = -1.1$ to reproduce our expected fraction of systems with detected planets.

We then explored other values of α in particular $\alpha = 0.0$ (a flat distribution of the planet mass distribution) and $\alpha = 1.3$.

For $\alpha = 0.0$, adopting the Cumming's value of the index $\beta = 0.6$ we would expecte a fraction of systems with detected planets of 10% for a cut-off semi-major axis of 20 AU. We can reject this prediction at a confidence level of $2\sigma - 3\sigma$.

In the last two plots, fixing $\alpha = 1.3$, we reject at a confidence level of 5σ the index $\beta = 0.6$ at a semi-major axis cut-off of 20AU. For all semi-major axes distribution of cut-off we exclude the possibility

to interpret our expected fraction of systems with detected planet with the Cumming's value of the index $\beta = 0.6$.

We conclude that the general trend when increasing α, i.e. increasing the proportion of high-mass planets, is to move towards smaller values for β, that is a lower number of giant planets at larger separations.

In the plots of Fig.17 we analysed the expected fraction of systems with detected planets as a function of the index α and of the semi-major axis cut-off, fixed the index β of the distribution of the semi-major axis.

Assuming the index $\beta = -1.60$, we have a high confidence level for rejection for all values of the semi-major axes cut-off when $\alpha = -1.31$ (dash line). For $\beta = -0.60$ (the Cummimg's value) the fraction of detection is within 1σ of confidence level of the expected value for a semimajor axis cutoff of 20AU. This suggests an even lower value for the cut-off.

In the last plot of Fig.17 most of region of the plane (α, cut-off) displayed a rejection level of 5σ. We conclude that increasing the parameter β, i.e. when increasing the proportion of planets at large orbital separations, the general trend of agreement with observations requires to move towards smaller values for α, that is, a lower number of massive giant planets.

Concluding all these plots show the unlikelihood to describe the distribution of the mass and the distribution of the semi-major axis of the giant planets at wide orbits using the Cumming's values for the indexes.

On the other hand, assuming an upper limit ≤ 10 AU, the power laws of Cumming et al. are in a reasonable agreement ($\sim 1\sigma$) with our fraction of detection. This can be understood if we consider the fact that the Cumming's indexes are obtained from the radial velocity method that it is appropriate to detect planets at small separations. Extrapolations of their power laws at large separations lead to overestimate the number of planets of large separations with respect to observations of the number of planets at large separations. Clearly, the distribution of planets curve separations has a maximum of a few AU (not far from the snow-line) and then decline outward. This is now a clear observed fact.

6.2.2 Comparison with Bryan et al. (2016)

Bryan et al. (2016) have recently conducted a Doppler survey at Keck, combined with NIRC2 K-band AO imaging, to search for massive, long-period companions to 123 known exoplanet systems

having one or two planets previously detected using the radial velocity (RV) method.

Their survey is sensitive to Jupiter mass planets out to 20 AU for a majority of the stars in their sample, and they combine their RV observations with AO imaging to determine the range of allowed masses and orbital separations for these companions.

They estimated that the total occurrence rate of companions in their sample is $52 \pm 5\%$ over the range $1 - 20 M_J$ and $5 - 20$AU.

They considered a star sample different from ours. In particular they have selected systems with at least one companion in the inner part, and included stars in a very wide range of ages. We note that working with an old system could give more time to the dynamical processes (migration, resonances, tidal forces) to act and so to alter the initial distribution of the masses and of the semi major axis.

They assumed that the companions are distributed in mass and semi-major axis space according to a double power law in analogy with Cumming et al (2008).

We note that due to the different definition of the mass distribution (per logarithmic units rather than per linear units), their original exponents differ by one unit from those of Cumming et al. The values we consider in this discussion have been already correct for this difference and are then not the original ones. We list in the Table 2 the Bryan's et al. indexes, according to the Cumming et al. definition, calculated in a range which includes our mass range $[5-15]$ M_J and our range of semi-major axes: $[5-20]$AU, $[5-50]$AU, $[5 - 80]$:

Table 2

	$5 - 20$ AU	$5 - 50$ AU	$5 - 100$ AU
$1 - 20$ M_J	$\alpha = -1.22$	$\alpha = -0.56$	$\alpha = -0.14$
	$\beta = 0.82$	$\beta = -0.44$	$\beta = -0.74$

In Fig.20 we present three plots of the expected fraction of the systems with detected planets analyzing both the values of the Cumming's et al. indexes (star symbol) and the values of Bryan's et al. indexes (rectangular symbol) with respect to our expected fraction of detected planets. In Fig.21 we present the respective contour plots of the confidence level. In these plots we are evaluating how much the extrapolations of the power-law distributions of Bryan et al. are consistent with our observations for three cut-off values of 20, 50 and 100 AU. We remind that our expected-fraction is represented

by the red line in these figures.

The general trend emerging from this comparison is a strong disagreement; the rejected confidence level is over 2σ. We also notice that in the same plots there is a considerable disagreement between Cumming's et al. indexes and Bryan's et al. ones.

The disagreement between our observations, both with the indexes of the power laws of Bryan et al. and with the indexes of the power laws of Cumming et al., show that these power laws cannot be extrapolated to describe the distribution of mass and separation of semi-major axis for a giant planets at large. We remind that our work is a preliminary analysis of the first part of SHINE survey and more statistically significant results will be available when the survey will be completed.

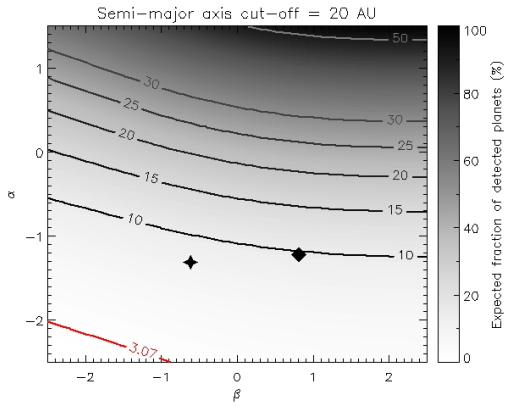

(a)

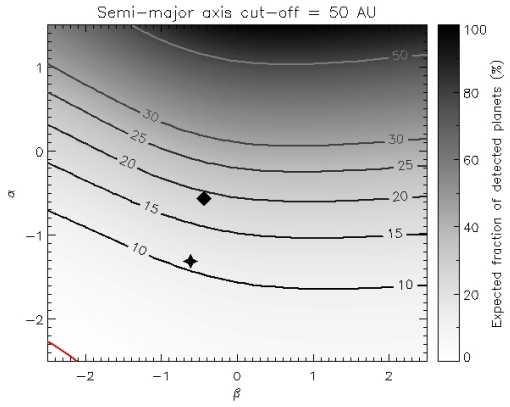

(b)

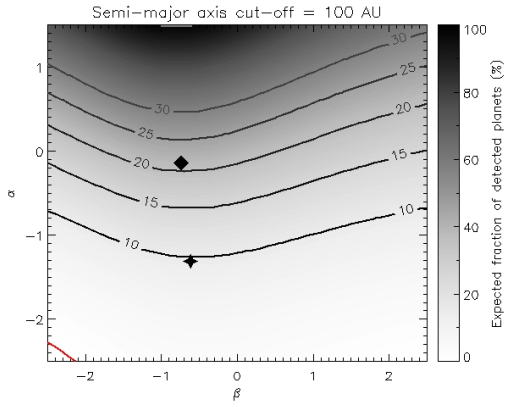

(c)

Figure 20: The expected fraction of the systems with detected planets. The star symbol is the value of α and β from Cumming et al. (2008) and the rectangular symbol is the value from Bryan et al. (2016) one.

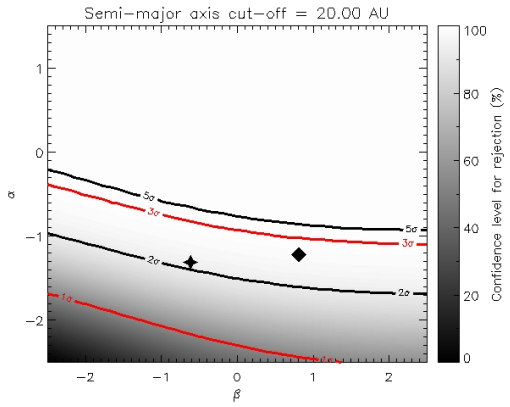

(a)

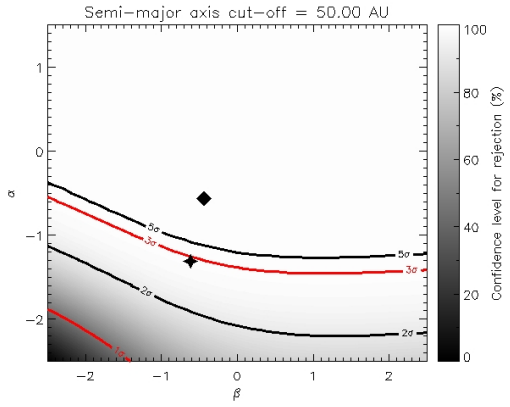

(b)

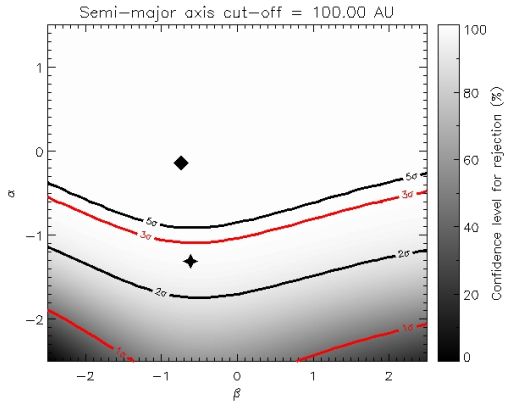

(c)

Figure 21: The contour plots of the confidence level respect our expected fraction of the systems with detected planets. The star symbol is the value of α and β from Cumming et al. (2008) and the rectangular symbol is the value from Bryan et al. 2016) one.

6.3 Overall frequency of giant planets

In the previous discussion we focused on the shape of the distributions with mass and semi-major axis of giant planets. We will now discuss what our data tells about the overall frequency of giant planets at large separations. In Fig. 22 we can compare the frequency of giant planets at large separations obtained from our sample (see Section 5.2) with the value given by the model presented by Bryan et al. for a semi-major axes cut-off of 20 AU. We have decided this value of semi-major axes cut-off for several reasons:

- The Bryan et al. survey is sensitive to Jupiter mass planets out to 20 AU; for values larger then this, their results are extrapolated.
- Inside this separation we have 3 confirmed detections.
- 20 AU represents a reasonable upper limit for a core-accretion scenario in a solar-type star.

Using a flat distribution for the masses and the semi-major axis and thus minimizing the dependence on the model, our interest is to understand how the results of Bryan et al. fit with our frequency.

We decided to calculate the expected fraction of planets through the Equation 6 (in Section 5) over the range $[5-15]M_J$ and $[5-20]$AU for which we have evaluated our frequencies. Using the Bryan et al. values for α and β we find a frequency of $f = 16 \pm 2\%$, represented by the yellow line in the Fig.20.

The lower limit of the 1σ confidence range of Bryan et al. is exactly over the upper 1σ limit of our frequency. We conclude that our results are (barely) compatible with those by Bryan et al., though they hint a lower frequency of planets at wide orbits. As mentioned our investigation is still preliminary: we expect at the end of the survey to reduce the error bars of our results. This will allow to better clarify if our results agree or less with those of Bryan et al. In particular, our sample has no assumptions on a companion at a small separation. For example, if an important fraction of the stars has no companion to any separation, this helps to lower the frequency of planets found in a sample like ours but has no effect on their results. So we expect a lower fraction than obtained by them. Furthermore, it is not for sure that the fraction of planets in large separations is independent of age.

We conclude that the two values are not inconsistent although there is a hint that our work is lower than Bryan et al. However, the difference is not orders of magnitude. We therefore expect the

fraction of systems with a giant planet, next to the snow-line, is of the order of several tens percent.

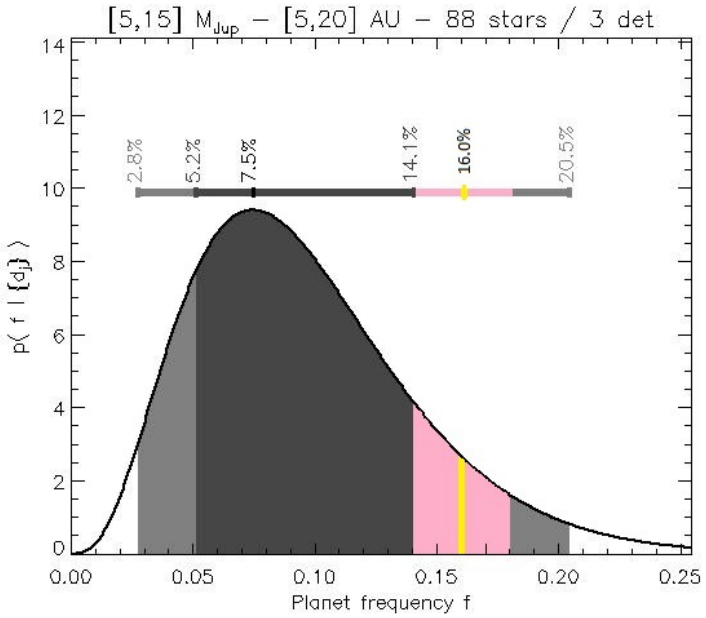

Figure 22: The probability density of f (posterior distribution), given the observations d_j, as a function of the planetary systems frequency f, in the semimajor axis interval [5-20] AU and a mass interval $[5-15]M_J$. The yellow line is the Bryan et al. value of the frequency.

7 Conclusions

The study and characterization of exoplanets is one of the most controversial topic in the astronomical research.

In this work we conducted a statistical analysis of 88 objects successfully observed with IFS (Integral-Field-Spectrograph) from the first ten months of the SHINE survey and leading to 12 candidates of which 4 were confirmed so far.

Our target selection is characterized by young ($\leq$ 500 Myr) and close to Earth ($\leq$ 170 pc) objects, in particular the ages of the observed stars are in the range of [1-500] Myr with a median value of 30 Myrs, the distribution of stellar distances is within 170 pc with a median value of 48.2 pc, and the range of mass is $[0.5 - 3]M_{\odot}$ with a median value of $1.22M_{\odot}$. A figure of merit was constructed for each individual target taking to consideration apparent magnitude, distance, age and spectral type. The highest figure of merit is attributed to those targets that have the highest probability of hosting a planet detectable by SPHERE according to power-law models. There is no assumption on the presence (or less) of a companion. Targets are then observed with a priority that depends on this figure of merit and on other a-priori criteria (membership to group, subdivision in mass ranges, etc.).

In first part of the statistical analysis we investigate with what confidence level the planet distributions obtained from RV surveys (Cumming et al. 2008 and Bryan et al 2016) can be extrapolated for planets at much larger orbital radii. We conclude that all our distributions show the unlikelihood (with a rejected confidence level over 2σ) to describe the distribution of the mass and the distribution of the semi-major axis of the giant planets at wide orbits using the Cumming's et al. and Bryan's et al. values for the indexes. Therefore, they show that these power laws cannot be extrapolated to describe the distribution of mass and separation of semi-major axis for a giant planet at large radii over a separation $\gtrsim$ 20AU and possibly less.

In the second part of the statistical analysis we estimate the frequency of exoplanetary systems in a mass interval of $[5 - 15]M_J$ for three semimajor axis intervals: $[5 - 20]$ AU, $[5 - 50]$ AU and $[5 - 100]$ AU. We compared this frequency with the value given by the model presented by Bryan et al. for a semi-major axes cut-off of 20 AU and for a range of mass of $[5 - 15]M_J$. We conclude that our results are (barely) compatible with those by Bryan et al., though they hint a lower frequency of planets at wide orbits. However our investigation is still preliminary and thus we expect at the end of

the survey to reduce the error bars of our results. This will allow to better clarify if our results agree or less with those of Bryan et al.

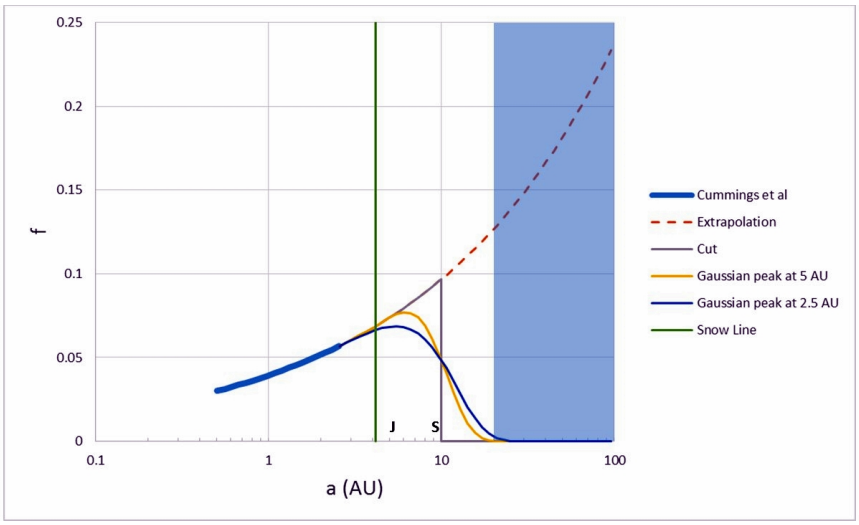

Figure 23: Run of the frequency of giant planets with separation (vertical scale) is arbitrary and the frequency is for logarithmic steps in separation. The thick solid blue line represents the result by Cummings et al. (2008) based on RV data. The dashed line is the extrapolation of the Cummings et al. result at large separation. The blue area represents the region where extrapolation of this relation is rejected by the SHINE data at more than 2σ level of confidence. The gray lines represent the upper cut for an extrapolation of the Cummings et al. data that gives a number of detections from the SHINE survey that is within 1σ of the observed value. Such a run is of course not physical. We then plot two lines which represent smooth distributions that are compatible with SHINE data that deviates from the Cumming et al. law at 2.5 AU (blue line) and 5.0 AU (yellow line). The vertical green line is at the snow-line for a median target in our survey. This is to show that the peak of distributions in agreement with RV and SHINE data should be slightly out of the snow-line. Finally, J and S represents the position of Jupiter and Saturn; these are clearly compatible with the peak of these distributions.

We can summarize all our statistical results through the graph in Figure 23. We note that the critical interval is $2.5AU < a_0 < 10AU$ and then we propose the following distribution for separation of the semi-major axis:

$$\frac{dn}{da} = a^{\beta} x \tag{7}$$

Where the parameter x is $x = 1$ for $a < a_0$ and $x = e^{-\frac{(a-a_0)^2}{2\sigma^2}}$ for $a > a_0$.

Therefore, for small separations ($a < a_0$) the distribution is represented by result based on RV data (Cummings et al. 2008) and for

$a > a_0$ we plot two lines which represent smooth possible distributions that are compatible with SHINE data. While arbitrary, these distributions give an idea of possible resonable extensions of the Cummings et al. relation. The peak of distribution, in agreement with RV and SHINE data, should be slightly out of the snow-line as predicted by the core accretion scenario.

In Figure 23, J and S represent the positions of Jupiter and Saturn; these are compatible with the peak of the overall distribution of giant planets, showing that on this respect the Solar System does not represent an exception.

Finally, being this an explorative analysis at wide orbits, we can qualitatively evaluate the efficiency of a scenario of giant planets formation at large orbits. Previous work (Matsuo et al.) have shown that only 10% of the giant planets is related to a scenario of disk instability, while 90% is due to the core accretion scenario. In this first part of the survey we can qualitatively evaluate a low efficiency of a giant planets formation at separation larger than 15 AU.

A Appendix

Expected fraction of detected planets as a function of the power law index α for the mass and the power law index β for the semi-major axis distributions, where the semi-major axis cut-off (a_{max}) of 10, 20, 30, 40 50, 60, 70, 80, 90, 100 are fixed. The star is the value of the indexes α and β distributions from Cumming et al. (2008) $\alpha = -1.31$ and $\beta = -0.65$. The rectangular symbol are the values of the indexes α and β distributions from Bryan et al. (2016).

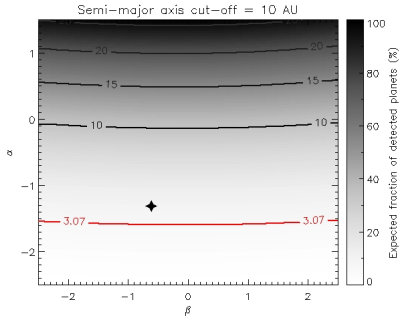

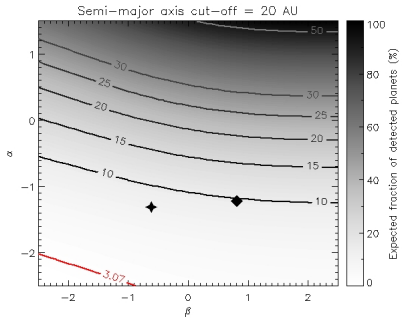

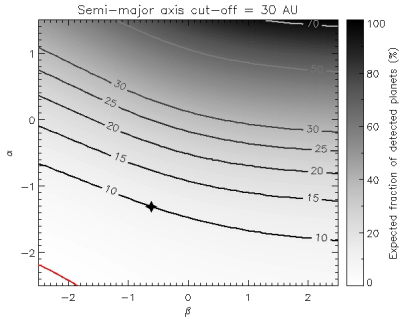

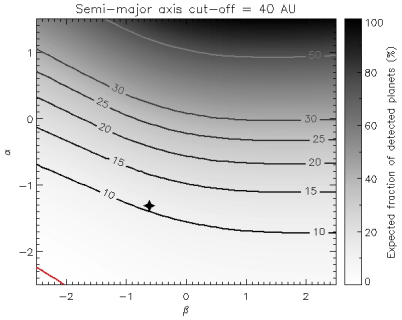
Semi−major axis cut−off = 40 AU
α
β
Expected fraction of detected planets (%)

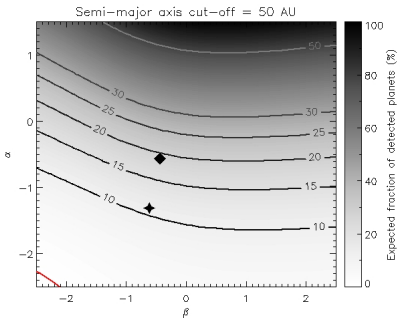
Semi−major axis cut−off = 50 AU
α
β
Expected fraction of detected planets (%)

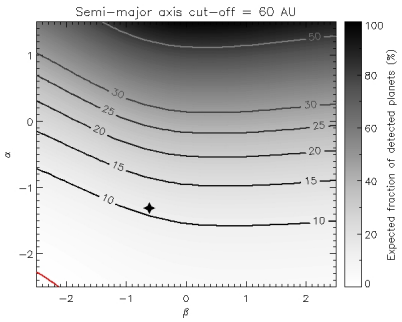
Semi−major axis cut−off = 60 AU
α
β
Expected fraction of detected planets (%)

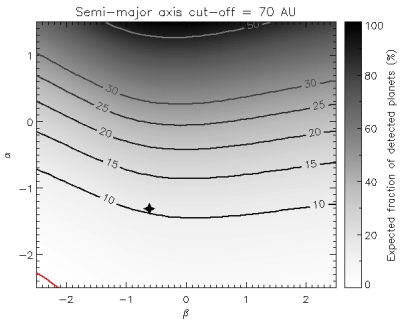
Semi−major axis cut−off = 70 AU
α
β
Expected fraction of detected planets (%)

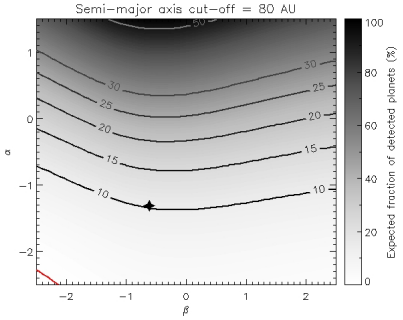
Semi−major axis cut−off = 80 AU
Expected fraction of detected planets (%)
α
β

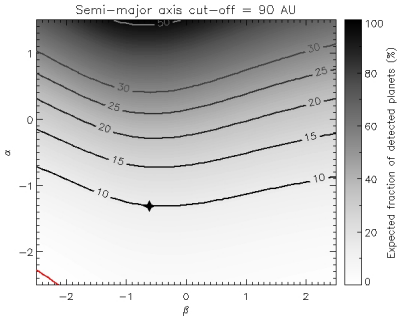
Semi−major axis cut−off = 90 AU
Expected fraction of detected planets (%)
α
β

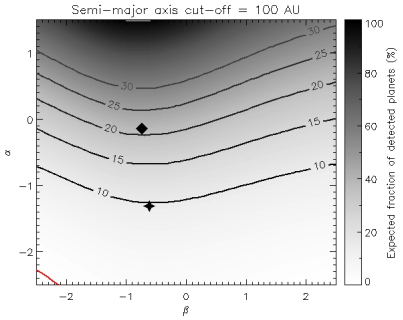
Semi−major axis cut−off = 100 AU
Expected fraction of detected planets (%)
α
β

B Appendix

In this Appendix I present the contour plots show the confidence level of 1σ, 2σ, 3σ and 5σ. The star symbol is the values of the indexes α and β distributions from Cumming et al. (2008) $\alpha = -1.31$ and $\beta = -0.65$. The rectangular symbol are the value of the indexes α and β distributions from Bryan et al. (2016).

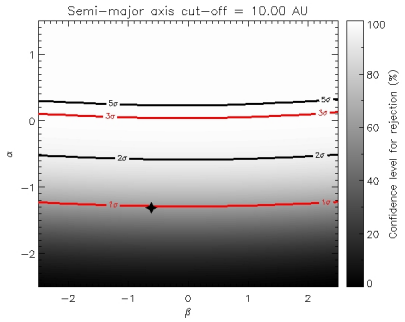

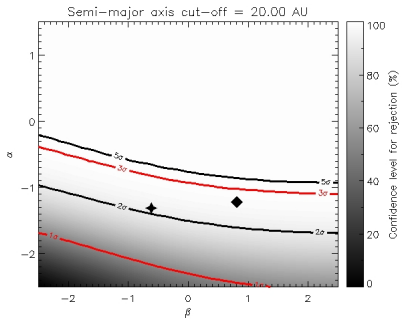

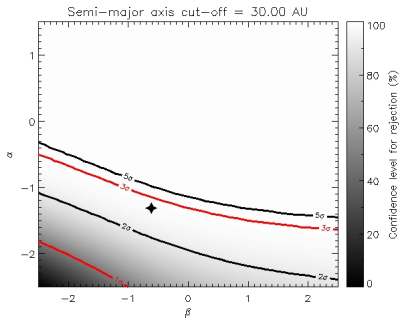

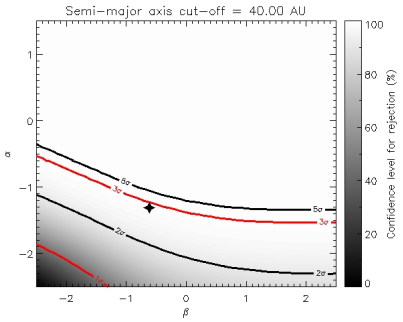
Semi-major axis cut-off = 40.00 AU
α
β
Confidence level for rejection (%)
5σ
3σ
2σ

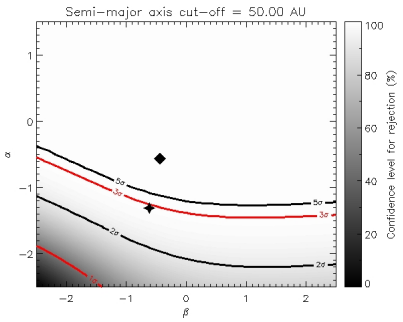
Semi-major axis cut-off = 50.00 AU
α
β
Confidence level for rejection (%)
5σ
3σ
2σ

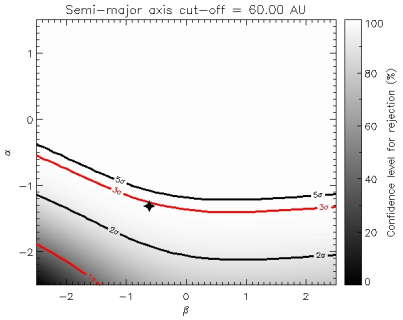
Semi-major axis cut-off = 60.00 AU
α
β
Confidence level for rejection (%)
5σ
3σ
2σ

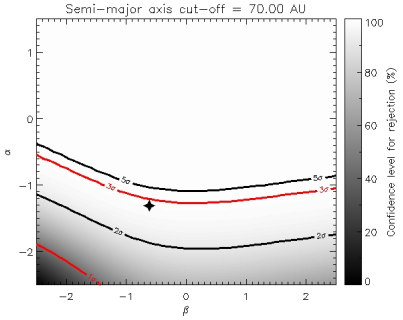
Semi-major axis cut-off = 70.00 AU
α
β
Confidence level for rejection (%)
5σ
3σ
2σ

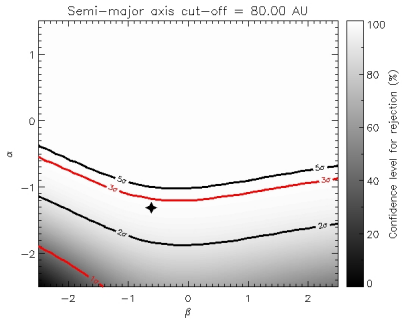
Semi−major axis cut−off = 80.00 AU
Confidence level for rejection (%)
α
β
5σ
3σ
2σ
1σ

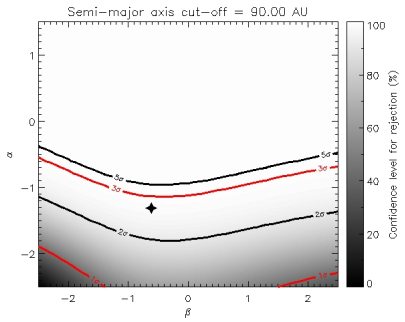
Semi−major axis cut−off = 90.00 AU
Confidence level for rejection (%)
α
β
5σ
3σ
2σ
1σ

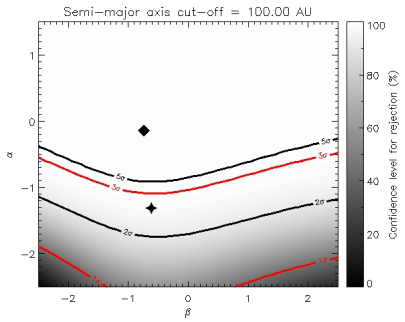
Semi−major axis cut−off = 100.00 AU
Confidence level for rejection (%)
α
β
5σ
3σ
2σ
1σ

References

[1] Armitage, P., J.,*Astrophysics of planet formation*, 2010, Cambridge University Press, pg. 185-216

[2] Baraffe, I., Chabrier, G., Barman, et al., 2003, A&A, 402, 701

[3] Baraffe, I., Chabrier, G., Barman, T. S., et al., 2003, A&A, 402, 701-712

[4] Beuzit, J. L., Feldt, M., Dohlen, K., et al. 2008, SPIE, 7014

[5] Bonavita, M., de Mooij, E. J. W., & Jayawardhana, R. 2013, PASP, 125, 849

[6] Bonnefoy, M., Marieau, G. D., Galicher, R., et al. 2014, A&A, accepted

[7] Boss, A. P., 1997, Science, 276, 1836

[8] Bryan, M. L., Knutson H A, Howard A W et al., 2016 ApJ, accepted

[9] Burrows, A., Marley, M., Hubbard, W. B., et al. 1997, ApJ, 491, 856

[10] Cameron, A. G. W. 1978, Moon and the Planets, 18, 5

[11] Carson, J. C., Eikenberry, S. S., Smith, J. J., et al 2006, AJ, 132, 1146

[12] Chauvin, G., Lagrange, A., Bonavita, M., et al. 2010, A&A, 509, A52

[13] Commercon, B., Audit, E., Chabrier, G., et al. 2011, A&A, 530, 13

[14] Cumming, A., Butler, R. P., Marcy, G. W., et al. 2008, PASP, 120, 531

[15] Dodson-Robinson, S., Ford, E., & Veras, D. 2009, ApJ, 707, 79

[16] Eisner, J. A., Hillenbrand, L. A., Carpenter, J. M., et al. 2005, ApJ, 635, 396

[17] Esposito S., Mesa D., Skemer A., et al. 2012, A&A., 459, A52

[18] Fischer, D.A. & Valenti, J. 2005, ApJ, 622,1102

[19] Fortney, J. J., Marley, M. S., Saumon, D., et al. 2008, ApJ, 683, 1104

[20] Ida, S., & Lin, D.N.C. 2004, ApJ, 604, 388

[21] Kalas P., Graham J. R., Chiang E., et al., 2008, Science, 322, 1345-1348; 2009

[22] Kasper, M., Apai, D., Janson, M., & Brandner, W. 2007, A&A, 472, 321

[23] Kratter, K. M., Murray-Clay, R. A., & Youdin, A. N. 2010, ApJ, 710, 1375

[24] Kuiper, G. P. 1951, Proceedings of the National Academy of Sciences, 37, 1

[25] Lafreniére, D., Jayawardhana, R., & van Kerkwijk, M. H. 2008, ApJ, 689, L153

[26] LafreniÃ¨re, D., Marois, C., Doyon, R., Nadeau, D., & Artigau, É. 2007b, ApJ, 660, 770

[27] Lagrange A. M., Bonnefoy M., Chauvin G., et al., 2010, Science, 329, 57.

[28] Lineweaver, C.H. & Grether 2003, D., ApJ, 598, 1350

[29] Macintosh, B., Graham, J., Barman, T., et al. 2015, Science, in press

[30] Marley, M. S., Fortney, J. J., Hubickyj, O., Bodenheimer, P. H., & Lissauer, J. J. 2007, ApJ, 655, 541

[31] Marois C., Macintosh B., Barman T., et al., 2008, Science, 322, 1348

[32] Mizuno, H. 1980, PTP, 64, 544

[33] Nielsen, E. L., & Close, L. M. 2010, ApJ, 717, 878

[34] Perri, F. & Cameron, A. G. W. 1974, Icarus, 22, 416

[35] Perryman M., 2000 Extra-solar planets. Rep. on Progress in Phys., 63, 1209

[36] Pollack, J B.; Hubickyj, O; Bodenheimer, P.; et al. 1996, Icarus, 124, 62

[37] Reggiani et al., 2016, A&A, 586, A147

[38] Santos N., et al, 2004, A&A, 426, L19

[39] Seager S., Exoplanets, 2010, University of Arizona Press, pg 111-120

[40] Spiegel, D. S. & Burrows, A. S. 2012, ApJ, 745, 174

[41] Zurlo, A; Bonnefoy, M, 2015, AAS, 47, 6